Mechanics of Time-Dependent Materials
https://doi.org/10.1007/s11043-024-09698-0

RESEARCH

Temperature-dependent thermal buckling and free vibration behavior of smart sandwich nanoplates with auxetic core and magneto-electro-elastic face layers

Kerim Gokhan Aktas[1] · **Fatih Pehlivan**[1] · **Ismail Esen**[1]

Received: 1 March 2024 / Accepted: 22 April 2024
© The Author(s) 2024

Abstract

This article addresses the thermomechanical thermal buckling and free vibration response of a novel smart sandwich nanoplate based on a sinusoidal higher-order shear deformation theory (SHSDT) with a stretching effect. In the proposed sandwich nanoplate, an auxetic core layer with a negative Poisson's ratio made of Ti-6Al-4V is sandwiched between Ti-6Al-4V rim layers and magneto-electro-elastic (MEE) face layers. The MEE face layers are homogenous volumetric mixtures of cobalt ferrite ($CoFe_2O_4$) and barium titanate ($BaTiO_3$). The mechanical and thermal material properties of the auxetic core and MEE face layers are temperature-dependent. Using Hamilton's principle, governing equations are constructed. To characterize the size-dependent behavior of the nanoplate, governing equations are adapted with the nonlocal strain gradient theory (NSGT). By applying the principles of Navier's technique, closed-form solutions are obtained. Parametric simulations are carried out to examine the effects of auxetic core parameters, temperature-dependent material properties, nonlocal parameters, electric, magnetic, and thermal loads on the free vibration and thermal buckling behavior of the nanoplate. According to the simulation results, it is determined that the auxetic core parameters, temperature-dependent material properties, and nonlocal factors significantly affect the thermomechanical behavior of the nanoplate. The outcomes of this investigation are expected to contribute to the advancement of smart nano-electromechanical systems, transducers, and nanosensors characterized by lightweight, exceptional structural integrity and temperature sensitivity. Also, the auxetic core with a negative Poisson's ratio provides a metamaterial feature, and thanks to this feature, the proposed model has the potential to be used as an invisibility technology in sonar and radar-hiding applications.

Keywords Auxetic core · Nonlocal strain gradient theory · Magneto-electro-elastic nanoplate · Cobalt ferrite · Barium titanate

✉ K.G. Aktas
kerimgokhanaktas@karabuk.edu.tr

[1] Engineering Faculty, Mechanical Engineering Department, Karabük University, 78050, Karabük, Turkey

Published online: 09 May 2024

1 Introduction

Auxetic structures characterized by a negative Poisson's ratio, a type of metamaterial, have found widespread use in structural applications due to their distinctive mechanical attributes such as ultra-lightweight, high strength-to-weight ratio, acoustic dampening, and enhanced energy absorption capacities (Nouraei and Zamani 2023). Under uniaxial compression conditions, auxetic structures undergo transverse contraction, while under uniaxial tension, they undergo transverse expansion (Ren et al. 2018). These unique characteristics of auxetic metamaterials make them suitable for potential uses including smart sensors, nano-electromechanical systems (NEMs), sonar systems, smart dampers, and acoustic isolators. The auxetic structures are lightweight and have a high shear modulus, but their mechanical performance is constrained by their low stiffness. In order to enhance the mechanical properties of auxetic structures, it has become essential to sandwich lightweight auxetic core layer between face layers that are more stiff. As face layers, piezoelectric plates, magneto-electro-elastic plates, and composite plates reinforced with carbon nanotubes (CNTs) or graphene platelets (GPLs) are frequently used (Fatih Pehlivan and Aktas 2024; Mahapatra et al. 2024; Nouraei and Zamani 2023). The integration of auxetic, honeycomb, and foam structures has been a subject of interest in various studies, shedding light on different aspects of their mechanical behavior and performance (Guo and Zhang 2023; Tian 2023; Xia et al. 2023; Zhang et al. 2022). Pawlus (2022) investigated the static stability of composite annular plates with auxetic properties, highlighting the composition of three-layered plates with auxetic facings and a soft foam core. This study provides insights into the structural behavior of plates with auxetic cores, offering valuable information for understanding the static performance of such composite structures. Janus-Michalska and Jasinska (2017) conducted a comparative study of the bending stiffness of sandwich plates with cellular cores, including those with cellular auxetic cores. By considering the bending behavior of plates with different core types, this study contributes to understanding the mechanical response of sandwich plates with auxetic cores, providing valuable insights into their structural performance. Furthermore, Mahesh (2023) delved into the integrated effects of auxetic and pyro-coupling on the nonlinear static behavior of MEE sandwich plates subjected to multifield interactive loads. Zhang et al. (2023b) presented an experimental investigation on the application of a carbon fiber-reinforced plastic plate to externally attach an advanced composite beam. While this study focused on MEE plates, it underscores the impact of blast loads on the dynamic behavior of plates with auxetic cores, offering valuable insights into the potential applications and performance of auxetic cores in sandwich structures under dynamic loading conditions.

Sandwich structures, a class of composite materials, have gained significant attention due to their versatile application in various engineering fields. These structures typically consist of two thin, stiff face sheets separated by a lightweight core material, forming a high-strength and lightweight configuration. The design of sandwich structures presents a unique challenge in load introduction, as highlighted by Janus-Michalska and Jasinska (2017), emphasizing the need for innovative concepts to efficiently distribute and manage loads within the structure. The mechanical behavior and stability of sandwich structures have been the focus of extensive research, with studies such as (Arefi et al. 2020) providing insights into the size-dependent free vibration analysis and stability of these structures. Additionally, the introduction of novel core materials, as demonstrated by Iftimiciuc et al. (2023), has further expanded the design possibilities and performance capabilities of sandwich structures. The unique properties of sandwich structures have led to diverse applications, ranging from flexible energy harvesters (Fu et al. 2020) to aerospace components (Joubaneh et al. 2018). Furthermore, the introduction of advanced materials and manufacturing techniques,

as explored by Wang et al. (2022) and Khan et al. (2017), has significantly enhanced the performance and functionality of sandwich structures. The introduction of innovative materials, such as graphene oxide and bismuth ferrite, has further expanded the capabilities of sandwich structures, as evidenced by studies from Yin et al. (2020) and Wu et al. (2011). In summary, sandwich structures represent a crucial area of research and development, with ongoing efforts focused on enhancing their mechanical properties, introducing novel materials, and exploring diverse applications across engineering disciplines (Sayyad and Avhad 2022; Shokravi and Jalili 2019; Tran et al. 2023; Wang et al. 2021).

MEE materials have gained significant attention due to their ability to convert one form of energy to another, their simple geometry, and their economic design, making them useful in smart or intelligent structure applications (Yildirim and Simsek 2022). These materials are composed of piezoelectric and piezomagnetic phases, and they have found vast applications in different industries owing to their predictable and controllable ability to couple different phases (Moshtagh et al. 2019). The mechanics of MEE composites have been extensively studied over the past few decades, with research focusing on various aspects such as wave propagation, vibration control, and free vibration analysis (Li et al. 2021; Vinyas et al. 2018; Zhang et al. 2020b; Zhou et al. 2020). Additionally, the development of new models, such as the microstructure-dependent anisotropic magneto-electro-elastic Mindlin plate model, has contributed to a deeper understanding of the behavior of MEE materials (Qu et al. 2020). Furthermore, MEE materials have been investigated for their potential applications in nanotechnology, with studies focusing on the vibration performance evaluation of smart magneto-electro-elastic nanobeams and the buckling analysis of magneto-electro-thermo-elastic cylindrical nanoshells (Gui and Li 2023; Liu and Lv 2019). The unique properties of MEE materials have also led to the development of new models, such as the transversely isotropic magneto-electro-elastic Timoshenko beam model, which incorporates microstructure and foundation effects, providing valuable insights for the design of MEE nanodevices (Wang and Jin 2022; Zhang et al. 2020a).

MEE materials at the microscale and nanoscale have gained significant attention due to their unique properties and potential applications. MEE materials exhibit coupling of mechanical, electrical, and magnetic fields, providing excellent magneto-electrical coupling at smaller scales (Ebrahimi and Barati 2017a). The smaller size and larger surface-to-volume ratio of MEE nanoscale structures have been noted to offer enhanced magneto-electrical coupling, making them suitable for applications in nano-electromechanical systems (NEMs) (Ebrahimi and Barati 2017a). Additionally, the material surface has been shown to have a marked effect on the mechanical behavior of MEE structures at the nanoscale (Wu et al. 2015). Classical theories are scale-free and fail to account for small scales. Moreover, these methods cannot accurately estimate the mechanical properties of nanostructures. The investigation of small-scale nonlocal impacts and size effects has been a key area of study for almost half a century, primarily through the nonlocal elasticity theory (NET) (Eringen and Wegner 2003; Eringen 1983a, 1972a,b; Eringen and Edelen 1972; Eringen and Suhubi 1964). Within this theory, the nonlocal parameter e_0a is precisely described. Both practical and theoretical research has demonstrated that the structure experiences a softening effect that is contingent upon the magnitude of this parameter. Subsequently, the impact of material size on microbeams was investigated using the strain gradient elasticity theory (SGT) (Kong et al. 2009; Wang et al. 2010). SGT (Kong et al. 2009, 2008a; Mindlin 1964), designed for small-scale systems, indicates the presence of a nonlocal characteristic that results in the substance becoming stiffer rather than softer. The property of being nonlocal is commonly known as the material size parameter. The modified coupled stress theory (MCST) was introduced with the advancement of the SGT (Kong et al. 2008b; Ma et al. 2008). MCST

(Şimşek and Reddy 2013; Yang et al. 2002) is explained by variables similar to the size parameter with an equivalent hardening influence. Due to scaling inconsistencies between nonlocal elasticity and strain gradient theories, a novel approach capable of capturing the two softening and hardening stiffness size impacts is required (Alghanmi 2023). Finally NSGT, which combines Eringen's nonlocal theory with the strain gradient elasticity theory, was developed (Alghanmi 2022; Ebrahimi and Barati 2017b; Li et al. 2015; Lim et al. 2015). In recent years, this theory has grown increasingly popular. Research has delved into various aspects of MEE materials at the micro and nanoscales, including wave propagation analysis, bending behavior, buckling analysis, and the development of exact solutions for different configurations (Hong et al. 2022; Pan 2001; Pan and Han 2005). Zhang et al. (2023a) showed unprecedented mechanical and microstructural features of advanced composites that include nanoparticles. Furthermore, the effective properties of MEE composites and the impact of interfacial cracks on their properties were investigated (Bhangale and Ganesan 2006; Huang et al. 2009). The potential applications of MEE materials in transducers, sensors, and actuators were highlighted, emphasizing their significance in various technological domains (Huang et al. 2009). Ferroelectric artificial application for high-performance neuromorphic computing was presented by Zhao et al. (2024), and tunable conductivity and ferromagnetism was studied by Guo et al. (2024). The interdisciplinary nature of this research, spanning physics, materials science, and engineering, underscores the significance of MEE materials in advancing technological innovation and addressing diverse engineering challenges. The development of novel formulations and exact solutions has enabled the analysis of MEE materials at the micro and nanoscales, contributing to the understanding of their mechanical behavior and potential applications (Pan and Han 2005; Yakhno 2018). In conclusion, extensive research on micro and nanoscale MEE materials has provided valuable insights into their behavior, properties, and potential applications. The unique coupling of mechanical, electrical, and magnetic fields in these materials has opened new avenues for technological advancements and the development of tailor-made materials with promising applications (Tiwari et al. 2021).

Extensive research has been conducted on functionally graded structures and functionally graded reinforced composite structures. These studies have particularly focused on the application of higher-order shear deformation theories, as evidenced by the literature (Alghanmi and Zenkour 2021; Daikh et al. 2023a,b, 2022; Koç et al. 2023; Melaibari et al. 2022; Özmen 2023; Saini and Pradyumna 2022; Yıldız and Esen 2023).

When employed at high temperature, MEE materials exhibit enhanced pyroelectric and pyromagnetic interactions. In addition, the mechanical, electrical, and magnetic characteristics of composite structures can change significantly with temperature. For this reason, it is essential to consider the temperature-dependent material attributes for the mechanical analysis of systems operated at high temperatures. The static reaction of a multilayer FG-MEE plate in a thermal environment was investigated by Vinyas and Kattimani (2017) for various temperature variations and boundary conditions utilizing the FEM. Additionally, Vinyas and Kattimani performed static deflection analysis of an FG-MEE structure using FEM under hygrothermal effects. Ebrahimi and Barati (2016a) used the HSDT to assess the impacts of distinct temperature distributions on the frequency performance of magneto-electro-thermo-elastic functionally graded (METE-FG) nanostructures. Ebrahimi and Barati (2016b) investigated the thermo-electro-mechanical buckling behavior of functionally graded piezoelectric (FGP) nanobeams with HSDT. Wang et al. (2023) conducted an investigation on the thermal properties of high-entropy RE-disilicates, which were regulated through high throughput composition design and optimization.

Having conducted an extensive review of the existing literature, it was concluded that the five-layer smart sandwich nanoplate with an auxetic core and MEE face layers is a

novel nanostructure that has not been previously investigated, particularly in relation to the temperature-dependent properties of the MEE face layers (BaTiO3 and CoFe2O4) and auxetic core layer. Thus, the temperature dependent free vibration and thermal buckling analysis of the presented sandwich smart nanoplate with a metamaterial property will be presented for the first time. Models developed by neglecting the auxetic core and MEE face layers's actual temperature behavior will produce inaccurate findings in practice because they do not accurately represent the physical behavior of the presented sandwich structure. Therefore, with this study, a model in which the thermomechanical properties of these materials are obtained through rigorous simulation studies has been created and presented to the reader. Auxetic core has a negative Poisson's ratio, and it can be adjusted with auxetic core parameters. This feature gives smart nanoplates additional metamaterial properties, and thanks to this feature, they provide potential for use in hiding applications from sonar and radar waves. Additionally, nano electromechanical systems that will operate in high noise environments have the potential to be used in sound or noise insulation applications. Moreover, they can be used in military applications such as impact dampening, target confusion, and personal protective equipment. This research aims to help understand the effect of auxetic core parameters (inclination angle, length of the horizontal wall, length of the inclined cell wall, and thickness of the cell wall), temperature-dependent material properties, nonlocal parameters, electric, magnetic, and thermal loads on the thermal buckling and free vibration characteristics of sandwich plate systems and to gain more insight into their possible applications in nanotechnology.

2 Theory and formulation

2.1 Summary of the suggested sandwich nanoplate

With this study, we consider a smart sandwich nanoplate with two MEE layers, an auxetic core layer, and two rim layers, which has length a, width b, and thickness h as illustrated in Fig. 1. x and y are in-plane axes located at the middle layer of the auxetic core, and z is the direction that extends along the thickness of the plate. h_s, h_r, and h_p are the thicknesses of the core layer, rim layer, and MEE layer, respectively.

The auxetic core layer with a negative Poisson's ratio is sandwiched between two MEE nanoplate layers and two metal rim layers. The materials used for the auxetic core and

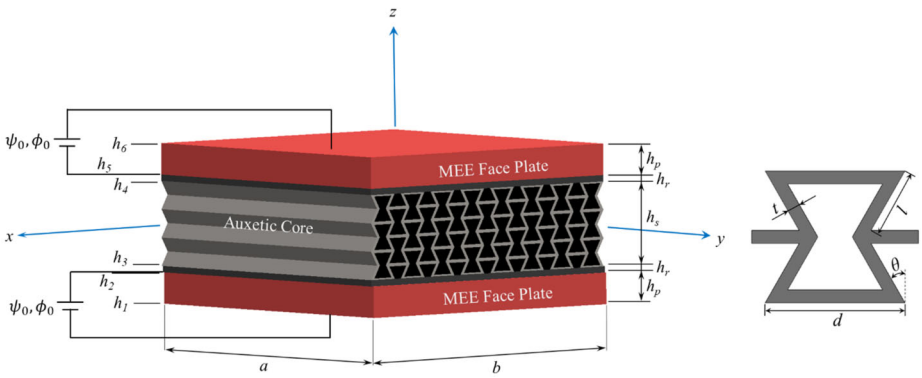

Fig. 1 An auxetic core sandwich nanoplate composed of thermo-magneto-electro-elastic face layers

rim layers are biocompatible material Ti-6Al-4V. In addition, $CoFe_2O_4$ and $BaTiO_3$ are considered to be homogeneously distributed in the MEE lower and upper face plates. Also, an external electrical voltage and magnetic field are applied through the thickness of the MEE layers, causing these layers to expand and contract along the z-axis.

2.2 Auxetic core

The core layer of the proposed sandwich plate is made of an auxetic material with a negative Poisson's ratio. The auxetic core layer consists of honeycomb cells placed in a systematic way, where θ, d, l, and t represent the angle of inclination, the length of the horizontal wall, the length of the inclined cell wall, and the thickness of the cell wall, respectively. The material properties such as Young modulus (E), shear modulus (G), and density (ρ) of the auxetic core can be expressed using the following equations (Li and Yuan 2022; Nouraei and Zamani 2023):

$$E_{11}^{C} = E_{Ti}\left[\frac{(\beta_1 - \sin\theta)\,\beta_3^3}{\left[\left(\beta_1 sec^2(\theta) + tan^2(\theta)\right)\beta_3^2 + 1\right] cos^3(\theta)}\right] \tag{1}$$

$$E_{22}^{C} = E_{Ti}\left[\frac{\beta_3^3}{\left(\beta_3^2 + tan^2(\theta)\right)(\cos(\theta)\,\beta_1 - \cos(\theta)\sin(\theta))}\right] \tag{2}$$

$$G_{12}^{C} = G_{Ti}\left[\frac{\beta_3^3}{\left(2\beta_1^2 + \beta_1\right)\cos\theta}\right] \tag{3}$$

$$G_{13}^{C} = G_{Ti}\left[\frac{2sin^2(\theta) + \beta_1}{2(\beta_1 - \sin(\theta))} + \frac{-\sin(\theta) + \beta_1}{2\beta_1 + 1}\right]\frac{\beta_3}{2\cos(\theta)} \tag{4}$$

$$G_{23}^{C} = G_{Ti}\left[\frac{\beta_3\cos(\theta)}{\beta_1 - \sin(\theta)}\right] \tag{5}$$

$$\rho^{C} = \rho_{Ti}\left[\frac{(2 + \beta_1)\,\beta_3}{2(\beta_1 - \sin(\theta))\cos(\theta)}\right], \tag{6}$$

in which $\beta_1 = d/l$ and $\beta_3 = t/l$. Also, the superscript c and subscript Ti represent the core layer and titanium, respectively. Furthermore, Poisson's ratio (v) can be derived from the geometric parameters in the form that follows (Li and Yuan 2022):

$$v_{12}^{C} = \frac{(\sin(\theta) - \beta_1)(\sin(\theta))\left(1 - \beta_3^2\right)}{\cos^2(\theta)\left[\beta_3^2\left(\beta_1 sec^2(\theta) + tan^2(\theta)\right) + 1\right]} \tag{7}$$

$$v_{21}^{C} = \frac{\left(\beta_3^2 - 1\right)\sin(\theta)}{(\beta_1 - \sin(\theta))\left(\beta_3^2 + tan^2(\theta)\right)}. \tag{8}$$

For the thermal expansion coefficients of the auxetic core, α_{11}^{C} and α_{22}^{C} can be described by (Hoang et al. 2023)

$$\alpha_{11}^{C} = \alpha_{Ti}\frac{\beta_3\cos(\theta)}{\beta_1 + \sin(\theta)}, \tag{9}$$

$$\alpha_{22}^{C} = \alpha_{Ti}\frac{\beta_3(\beta_1 + \sin(\theta))}{(2\beta_1 + 1)\cos(\theta)}. \tag{10}$$

2.3 Magneto-electro-elastic face layers

The mechanical, electrical, thermal, and magnetic properties of the face plates vary uniformly with volumetric ratio of $CoFe_2O_4$ and $BaTiO_3$ along the z-axis. Using the rule of mixture, the effective material parameters of MEE face layers can be defined as follows (Amini et al. 2015):

$$\begin{aligned} P_{eff}^{lp}(z) &= C_f P_C + B_f P_B, \quad h_1 \leq z \leq h_2, \\ P_{eff}^{up}(z) &= C_f P_C + B_f P_B, \quad h_5 \leq z \leq h_6, \\ C_f + B_f &= 1, \end{aligned} \tag{11}$$

where $P_{eff}(z)$ defines the effective material parameters, including the modulus of elasticity E, mass density ρ, Poisson's ratio υ, piezoelectric stress coefficient e, and dielectric constant ε. The length from the neutral plane is represented by z; C_f and B_f are the volumetric ratios of $CoFe_2O_4$ and $BaTiO_3$, respectively; P_C and P_B define the properties of $CoFe_2O_4$ and $BaTiO_3$ for the upper and lower face layers, respectively; and superscripts up and lp are the upper MEE plate and lower MEE plate, respectively.

Both the host structure and the face layers have temperature-dependent material characteristics that can be described by a nonlinear temperature equation, involving the modulus of elasticity E, Poisson's ratio ν, thermal conductivity ψ, and thermal expansion κ (Reddy and Chin 1998; Touloukian 1967, 1966):

$$P = P_0 \left(P_{-1} T^{-1} + 1 + P_1 T + P_2 T^2 + P_3 T^3 \right). \tag{12}$$

Here, P represents any temperature-dependent material coefficient. Table 1 lists the properties of $CoFe_2O_4$ and $BaTiO_3$ as a function of temperature, whereas Table 2 lists the properties of Ti-6Al-4V as a function of temperature. The temperature-dependent thermomechanical coefficients given in Table 1 for $CoFe_2O_4$ and $BaTiO_3$ were obtained as a result of partial experimental studies in the literature (Reddy and Chin 1998; Touloukian 1967), and from the analysis and simulations conducted and developed in this study.

2.4 Temperature increment on the sandwich nanoplate

In this subsection, we present the relevant formulations for three different types of temperature rises throughout the nanoplate: uniform (UTR), linear (LTR), and nonlinear (NLTR). A nanoplate with an initial temperature of $T_0 = 300K$ is consistently increased to its peak temperature T with a uniform temperature rise (UTR) using the following equation (Özmen and Esen 2023):

$$\Delta T = T - T_0. \tag{13}$$

The temperature of a horizontal surface that extends in the z-axis with the temperatures of its lower and upper surfaces T_b and T_t, respectively, can be calculated as follows, assuming that the temperature rises linearly (LTR) from T_b to T_t through the thicknesses (Kiani and Eslami 2013):

$$T(z) = T_b + (T_t - T_b) \left(\frac{h + 2z}{2h} \right). \tag{14}$$

Table 1 Temperature-dependent material coefficients for $CoFe_2O_4$ and $BaTiO_3$ (Koç et al. 2023)

Material	Properties	P_{-1}	P_0	P_1	P_2	P_3
$CoFe_2O_4$	C_{11} (Pa)	0	298.87×10^9	-1.552×10^{-4}	6.125×10^9	-9.0×10^{-11}
	C_{55} (Pa)	0	47.33×10^9	-1.552×10^{-4}	6.125×10^9	-9.0×10^{-11}
	υ	0	0.3	0	0	0
	$\alpha\left(1\mathrm{K}^{-1}\right)$	0	7.5×10^{-6}	-3.01×10^{-4}	4.02×10^{-6}	-1.01×10^{-9}
	κ (W/mK)	0	4.7030	-0.0011	1.6612×10^{-6}	-9.9670×10^{-9}
	ρ (kg/m^3)	0	5300	0	0	0
$BaTiO_3$	C_{11} (Pa)	0	174×10^9	-1.552×10^{-4}	6.125×10^{-9}	-9.0×10^{-11}
	C_{55} (Pa)	0	44.93×10^9	-1.552×10^{-4}	6.125×10^{-9}	-9.0×10^{-11}
	υ	0	0.30	0	0	0
	$\alpha\left(1\mathrm{K}^{-1}\right)$	0	10×10^{-6}	-3.0×10^{-4}	4.0×10^{-6}	-1.0×10^{-9}
	κ (W/mK)	0	3.7624	-8.50521×10^{-4}	1.32894ex10^{-6}	-7.97363×10^{-10}
	ρ (kg/m^3)	0	5800	0	0	0

Table 2 Temperature-dependent material coefficients of Ti-6Al-4V (Reddy and Chin 1998)

Material	Properties	P_{-1}	P_0	P_1	P_2	P_3
Ti-6Al-4V	E (Pa)	0	122.56×10^9	-4.586×10^{-4}	0	0
	υ	0	0.2884	1.121×10^{-4}	0	0
	$\alpha\left(1\mathrm{K}^{-1}\right)$	0	7.5788×10^{-6}	6.638×10^{-4}	-3.147×10^{-6}	0
	κ (W/mK)	0	1	1.704×10^{-2}	0	0
	ρ (kg/m^3)	0	4512	0	0	0

In the presence of a nonlinear temperature increase (NLTR) across the thickness direction of the nanoplates, the one-dimensional heat transfer problem given below can be addressed with specific temperature boundary limits to figure out the upper and lower surface temperatures (T_t and T_b) of the plate (Zhang 2014).

$$-\frac{d}{dz}\left(\kappa\left(z\right)\frac{dT}{dz}\right)=0, \qquad T\left(\frac{h}{2}\right)=T_t, \qquad T\left(-\frac{h}{2}\right)=T_b. \tag{15a}$$

Here, $\kappa\left(z\right)$ denotes the thermal conductivity coefficient. For a given boundary condition, the temperature of any point through the thickness z-axis can be calculated as follows (Esen and Özmen 2022a):

$$T\left(z\right)=T_b+\frac{\left(T_t-T_b\right)}{\int_{-\frac{h}{2}}^{\frac{h}{2}}\frac{1}{\kappa(z)}d\left(z\right)}\int_{-\frac{h}{2}}^{z}\kappa\left(z\right)dz. \tag{15b}$$

2.5 Application of nonlocal strain gradient theory to MEE sandwich nanoplates

According to Eringe's work (Eringen 1983b), the stress at any place on the structure is a function of the stresses at all points in the body. In this theory, the stiffness of the body depends on the strength of the nonlocal and material scale effects. In proportion to the strength

of the nonlocal effect, the structure acts in a manner that is less rigid than traditional forms. On the other hand, the SGT presumes that just the material scale effect, which contributes to an increase in the object's stiffness, is taken into consideration. In conclusion, Eringen's NETs and SGTs illustrate two separate material properties. The NSGT models nonlocal effects by combining these two distinct effects into a single effect (Li et al. 2016; Lim et al. 2015). In the NSGT, the stress can be calculated as (Lim et al. 2015)

$$\sigma = \int_V \alpha_0(\boldsymbol{x}', \boldsymbol{x}, e_0 a)\boldsymbol{C} : \varepsilon'\left(\boldsymbol{x}'\right) dV', \tag{16}$$

$$\sigma^{(h)} = l_m^2 \int_V \alpha_1(\boldsymbol{x}', \boldsymbol{x}, e_1 a)\boldsymbol{C} : \nabla\varepsilon'(\boldsymbol{x}')dV', \tag{17}$$

where $e_0 a$ and $e_1 a$ represent the nonlocality constants with e_1 and e_0 material coefficients, and α_0 and α_1 are the kernel and higher-order nonlocal functions, respectively. $\boldsymbol{C}$ and ∇ represent the fourth-order material coefficient and Laplacian operator $(\nabla = \partial/\partial x + \partial/\partial y)$, respectively. $\nabla\varepsilon$ and ε are the strain tensor and the strain gradient, respectively. l_m is the material length size factor. The stress tensor can be expressed as follows based on the NSGT (Farajpour and Rastgoo 2017; Lim et al. 2015):

$$\sigma^t = \sigma - \nabla^2\sigma^{(1)}. \tag{18}$$

By using the notations given in Ref. (Eringen 1983a) for $\alpha_1(\boldsymbol{x}', \boldsymbol{x}, e_1 a)$ and $\alpha_0(\boldsymbol{x}', \boldsymbol{x}, e_0 a)$, and assuming $e_0 = e_1 = e_0 a$, utilizing the linear differentiation operator to Eq. (18) gives

$$\left[1 - (e_0 a)^2\nabla^2\right]\sigma = \mathrm{C} : \varepsilon, \tag{19}$$

$$\left[1 - (e_0 a)^2\nabla^2\right]\sigma^{(1)} = l_m^2\mathrm{C} : \nabla\varepsilon. \tag{20}$$

Using Eqs. (18)–(20), the total stress can be obtained as follows:

$$\left[1 - (e_0 a)^2\nabla^2\right]\sigma = \mathrm{C} : \varepsilon - l_m^2\nabla\mathrm{C} : \nabla\varepsilon. \tag{21}$$

The stress–strain relations of the plate structure are defined by (Li et al. 2016; Lim et al. 2015)

$$\begin{aligned}
\left[1 - (e_0 a)^2\nabla^2\right]\sigma_{xx} &= \left[1 - l_m^2\nabla^2\right]E(z)\varepsilon_{xx} \\
\left[1 - (e_0 a)^2\nabla^2\right]\sigma_{yy} &= \left[1 - l_m^2\nabla^2\right]E(z)\varepsilon_{yy} \\
\left[1 - (e_0 a)^2\nabla^2\right]\sigma_{xz} &= \left[1 - l_m^2\nabla^2\right]G(z)\gamma_{xz} \\
\left[1 - (e_0 a)^2\nabla^2\right]\sigma_{yz} &= \left[1 - l_m^2\nabla^2\right]G(z)\gamma_{yz}
\end{aligned} \tag{22}$$

where σ_{xx}, σ_{yy} and ε_{xx}, ε_{yy}, represent the stresses and strains, respectively. Additionally, σ_{xz}, σ_{yz}, γ_{xz}, and γ_{yz} represent the shear stresses and strains, respectively. $E\ (z)$ is the Young modulus, while $G\ (z)$ is the shear modulus. As a result, taking into account the MEE characteristics of the NGST nanostructure under thermal effects may be expressed as follows (Eringen 1983a):

$$\boldsymbol{\sigma}\ (x, y, z)\left(1 - e_0 a^2\nabla^2\right) = \left(1 - l_m^2\nabla^2\right)\left[\overline{\boldsymbol{C}}\ (z)\,\boldsymbol{\varepsilon} - \overline{\boldsymbol{e}}\ (z)\,\boldsymbol{E} - \overline{\boldsymbol{q}}\ (z)\,\boldsymbol{H}\right] - \overline{\boldsymbol{C}}\ (z)\,\alpha\ (z)\,\Delta T$$

$$\boldsymbol{D}(x,y,z)\left(1-e_0a^2\nabla^2\right)=\left(1-l_m^2\nabla^2\right)\left[\overline{\boldsymbol{e}}^{\mathrm{T}}(z)\,\boldsymbol{\varepsilon}-\overline{\boldsymbol{\varepsilon}}(z)\,\boldsymbol{E}+\overline{\mathbf{g}}(z)\,\boldsymbol{H}\right] \tag{23}$$
$$\boldsymbol{B}(x,y,z)\left(1-e_0a^2\nabla^2\right)=\left(1-l_m^2\nabla^2\right)\left[\overline{\boldsymbol{q}}^{\mathrm{T}}(z)\,\boldsymbol{\varepsilon}+\overline{\mathbf{g}}(z)\,\boldsymbol{E}+\overline{\boldsymbol{\mu}}(z)\,\boldsymbol{H}\right],$$

where e, q, ε, g, and μ represent the piezoelectric, magneto strictive, dielectric, magneto-electric, and magnetic permeability constants, respectively; E, H, D, and B denote the electrical field, magnetic field, electrical displacement, and magnetic induction, respectively. The mechanical, electrical, magnetic, and thermal material properties of $CoFe_2O_4$ and $BaTiO_3$ are presented in Table 3.

2.6 Displacement fields and strains

The sinusoidal high-order shear deformation theory was applied to the five-layer sandwich nanoplate presented in this study under the following assumptions (Żur et al. 2020):

1. Because the displacements are small compared to the thickness of the plate, the strains involved are also very small.
2. The in-plane displacements u and v comprise extension u_0, bending w_b, and shear w_s components, respectively.
3. The transverse strains (ε_{xz}, ε_{yz}, ε_{zz}) and stresses (σ_{xz}, σ_{yz}, σ_{zz}) are considered as a result of the transverse displacement w, which includes components of bending w_b, shear w_s, and stretching w_{st}.
4. Including the shear components (w transverse displacements and w_{st} in v, u in-plane) leads to a rise in the trigonometric variation of the shear stresses (σ_{xz}, σ_{yz}) and strains (ε_{xz}, ε_{yz}) throughout the thickness of the plate. Consequently, the plate's top and bottom faces experience no shear stresses (σ_{xz}, σ_{yz}).

By using SHSDT, the nanoplate's displacement field is described as follows (Żur et al. 2020):

$$u(x,y,z,t)=u_0(x,y,t)-z\frac{\partial w_b(x,y,t)}{\partial x}-f(z)\frac{\partial w_s(x,y,t)}{\partial x}, \tag{24a}$$

$$v(x,y,z,t)=v_0(x,y,t)-z\frac{\partial w_b(x,y,t)}{\partial y}-f(z)\frac{\partial w_s(x,y,t)}{\partial y}, \tag{24b}$$

$$w(x,y,z,t)=w_b(x,y,t)+w_s(x,y,t)+w_{st}(x,y,z,t), \tag{24c}$$

where u, v, and w are the movements of any point in the x, y, and z axes, respectively. w_b, w_s, and w_{st} represent bending, shear, and stretching, respectively. Additionally, u_0, v_0, and w_b are the displacements of the mid-plane. Here, $f(z)$, w_{st}, and $g(z)$ are defined as (Tahir et al. 2021)

$$f(z)=z-\frac{2z\sin\left(\frac{z^2}{h^2}\right)}{2\sinh\left(\frac{1}{4}\right)+\cosh\left(\frac{1}{4}\right)}, \tag{25}$$

$$w_{st}(x,y,z,t)=g(z)\,\emptyset(x,y,t), \tag{26}$$

$$g(z)=\frac{df(z)}{dz}. \tag{27}$$

Table 3 Electromechanical material properties of $CoFe_2O_4$ and $BaTiO_3$ (Esen and Özmen 2022b)

Properties	$CoFe_2O_4$	$BaTiO_3$
Elastic constants (GPa)		
$C_{11} = C_{22}$	286	166
C_{33}	269.5	162
C_{12}	173	77
$C_{13} = C_{23}$	170.5	78
$C_{44} = C_{55}$	45.3	43
C_{66}	56.5	44.5
Piezoelectric constants (C/m^2)		
$e_{31} = e_{32}$	0	−4.4
$e_{15} = e_{24}$	0	–
e_{33}	0	−18.6
Dielectric constants (nF/m)		
$\xi_{11} = \xi_{22}$	0.08	11.2
ξ_{33}	0.093	12.6
Magnetic constants (N/A.m)		
$q_{31} = q_{32}$	580.3	0
q_{33}	699.7	0
Magnetic permeability (10^{-6} Ns^2/C)		
$\chi_{11} = \chi_{22}$	590	5
χ_{33}	157	10
Pyroelectric constant (10^{-7} C/m^{2}K)		
$p_{11} = p_{22}$	0	0
p_{33}	0	−11.4
Pyromagnetic constant (10^{-5} C/m^{2}K)		
$\lambda_{11} = \lambda_{22}$	0	0
λ_{33}	−36.2	0
Thermal expansion coefficient (10^{-6}K^{-1})		
$\alpha_{11} = \alpha_{22}$	10	15.8
Density (kg/m^3)		
ρ	5300	5800

The displacement field in Eq. (24a)–(24c) is related to the strain-displacement interactions, which have the following general form (Żur et al. 2020):

$$\begin{Bmatrix} \varepsilon_{xx} \\ \varepsilon_{yy} \\ 2\varepsilon_{xy} \end{Bmatrix} = \begin{Bmatrix} \varepsilon_{xx}^{(0)} \\ \varepsilon_{yy}^{(o)} \\ \gamma_{xy}^{(0)} \end{Bmatrix} + z \begin{Bmatrix} \varepsilon_{xx}^{(b)} \\ \varepsilon_{yy}^{(b)} \\ \gamma_{xy}^{(s)} \end{Bmatrix} + f(z) \begin{Bmatrix} \varepsilon_{xx}^{(s)} \\ \varepsilon_{yy}^{(s)} \\ \gamma_{xy}^{(s)} \end{Bmatrix} \tag{28a}$$

$$\begin{Bmatrix} 2\varepsilon_{xz} \\ 2\varepsilon_{yz} \end{Bmatrix} = g(z) \begin{Bmatrix} \gamma_{xz}^{(0)} \\ \gamma_{yz}^{(0)} \end{Bmatrix} \tag{28b}$$

$$\varepsilon_{zz} = g'(z)\varepsilon_{zz}^{(0)}. \tag{28c}$$

The spatial derivative of $g(z)$ with respect to z is represented here by $g'(z)$. The specific strain elements can be written as follows:

$$\begin{Bmatrix} \varepsilon_{xx}^{(0)} \\ \varepsilon_{yy}^{(0)} \\ \gamma_{xy}^{(0)} \end{Bmatrix} = \begin{Bmatrix} \dfrac{\partial u_0}{\partial x} \\ \dfrac{\partial v_0}{\partial y} \\ \dfrac{\partial u_0}{\partial y} + \dfrac{\partial v_o}{\partial x} \end{Bmatrix}, \qquad \begin{Bmatrix} \varepsilon_{xx}^{(b)} \\ \varepsilon_{yy}^{(b)} \\ \gamma_{xy}^{(b)} \end{Bmatrix} = \begin{Bmatrix} -\dfrac{\partial^2 w_b}{\partial x^2} \\ -\dfrac{\partial^2 w_b}{\partial y^2} \\ -2\dfrac{\partial^2 w_b}{\partial x \partial y} \end{Bmatrix} \tag{29a}$$

$$\begin{Bmatrix} \varepsilon_{xx}^{(s)} \\ \varepsilon_{yy}^{(s)} \\ \gamma_{xy}^{(s)} \end{Bmatrix} = \begin{Bmatrix} -\dfrac{\partial^2 w_s}{\partial x^2} \\ -\dfrac{\partial^2 w_s}{\partial y^2} \\ -2\dfrac{\partial^2 w_s}{\partial x \partial y} \end{Bmatrix} \tag{29b}$$

$$\begin{Bmatrix} \gamma_{xz}^{(0)} \\ \gamma_{yz}^{(o)} \end{Bmatrix} = \begin{Bmatrix} \left(1 - f'(z)\right)\dfrac{\partial w_s}{\partial x} + g(z)\dfrac{\partial \emptyset}{\partial x} \\ \left(1 - f'(z)\right)\dfrac{\partial w_s}{\partial y} + g(z)\dfrac{\partial \emptyset}{\partial y} \end{Bmatrix} = \begin{Bmatrix} g(z)\left(\dfrac{\partial w_s}{\partial x} + \dfrac{\partial \emptyset}{\partial x}\right) \\ g(z)\left(\dfrac{\partial w_s}{\partial y} + \dfrac{\partial \emptyset}{\partial y}\right) \end{Bmatrix}.$$

2.7 Constitutive equations

In this study, an auxetic core is considered to be sandwiched between orthotropic piezomagnetic face layers and isotropic rim layers. Using the differential form of Eringen's constitutive relations, we can formulate the following definitions of the auxetic core (s) and rim layer (r) (Żur et al. 2020):

$$\begin{Bmatrix} \mathcal{L}(\sigma_{xx}) \\ \mathcal{L}(\sigma_{yy}) \\ \mathcal{L}(\sigma_{zz}) \\ \mathcal{L}(\sigma_{yz}) \\ \mathcal{L}(\sigma_{xz}) \\ \mathcal{L}(\sigma_{xy}) \end{Bmatrix}^{s,r} = \begin{bmatrix} C_{11} & C_{12} & C_{13} & 0 & 0 & 0 \\ C_{12} & C_{22} & C_{23} & 0 & 0 & 0 \\ C_{13} & C_{23} & C_{33} & 0 & 0 & 0 \\ 0 & 0 & 0 & C_{44} & 0 & 0 \\ 0 & 0 & 0 & 0 & C_{55} & 0 \\ 0 & 0 & 0 & 0 & 0 & C_{66} \end{bmatrix}^{s,r} \begin{Bmatrix} \varepsilon_{xx} \\ \varepsilon_{yy} \\ \varepsilon_{zz} \\ 2\varepsilon_{yz} \\ 2\varepsilon_{xz} \\ 2\varepsilon_{xy} \end{Bmatrix}. \tag{30}$$

Here, C_{ij}^{n} represents the elastic constant and can be calculated as follows:

$$C_{11}^{s,r} = \frac{1-v}{v}\lambda(z) \tag{31a}$$

$$C_{12}^{s,r} = \lambda(z) \tag{31b}$$

$$C_{66}^{s,r} = \mu(z) \tag{31c}$$

$$C_{11}^{s,r} = C_{22}^{s,r} = C_{33}^{s,r} \tag{31d}$$

$$C_{12}^{s,r} = C_{13}^{s,r} = C_{23}^{s,r} \tag{31e}$$

$$C_{44}^{s,r} = C_{55}^{s,r} = C_{66}^{s,r}, \tag{31f}$$

where $\lambda(z)$ and $\mu(z)$ are the Lamé constants $\left(\lambda(z) = \frac{vE(z)}{(1+v)(1-2v)},\ \mu(z) = \frac{E(z)}{2(1+v)}\right)$.

The MEE face layer (p) constitutive relations are provided by Pan and Heyliger (2002) using nonlocal and strain-gradient differential operators. $\mathcal{L}(*) \equiv 1 - (e_0 a)^2 \nabla^2$ and $\Gamma(*) \equiv 1 - (l_m)^2 \nabla^2$.

$$\begin{Bmatrix} \mathcal{L}(\sigma_{xx}^p) \\ \mathcal{L}(\sigma_{yy}^p) \\ \mathcal{L}(\sigma_{zz}^p) \\ \mathcal{L}(\sigma_{yz}^p) \\ \mathcal{L}(\sigma_{xz}^p) \\ \mathcal{L}(\sigma_{xy}^p) \end{Bmatrix} = \Gamma \begin{bmatrix} C_{11}^p & C_{12}^p & C_{13}^p & 0 & 0 & 0 \\ C_{12}^p & C_{22}^p & C_{23}^p & 0 & 0 & 0 \\ C_{13}^p & C_{23}^p & C_{33}^p & 0 & 0 & 0 \\ 0 & 0 & 0 & C_{44}^p & 0 & 0 \\ 0 & 0 & 0 & 0 & C_{55}^p & 0 \\ 0 & 0 & 0 & 0 & 0 & C_{66}^p \end{bmatrix} \begin{Bmatrix} \varepsilon_{xx} \\ \varepsilon_{yy} \\ \varepsilon_{zz} \\ 2\varepsilon_{yz} \\ 2\varepsilon_{xz} \\ 2\varepsilon_{xy} \end{Bmatrix}$$
$$- \Gamma \begin{bmatrix} 0 & 0 & e_{31} \\ 0 & 0 & e_{32} \\ 0 & 0 & e_{33} \\ 0 & e_{24} & 0 \\ e_{15} & 0 & 0 \\ 0 & 0 & 0 \end{bmatrix} \begin{Bmatrix} E_x \\ E_y \\ E_z \end{Bmatrix} - \Gamma \begin{bmatrix} 0 & 0 & q_{31} \\ 0 & 0 & q_{32} \\ 0 & 0 & q_{33} \\ 0 & q_{24} & 0 \\ q_{15} & 0 & 0 \\ 00 & 0 & \end{bmatrix} \begin{Bmatrix} H_x \\ H_y \\ H_z \end{Bmatrix} \tag{32a}$$

$$\begin{Bmatrix} \mathcal{L}(D_x) \\ \mathcal{L}(D_y) \\ \mathcal{L}(D_z) \end{Bmatrix} = \Gamma \begin{bmatrix} 0 & 0 & 0 & 0 & e_{15} & 0 \\ 0 & 0 & 0 & e_{24} & 0 & 0 \\ e_{31} & e_{32} & e_{33} & 0 & 0 & 0 \end{bmatrix} \begin{Bmatrix} \varepsilon_{xx} \\ \varepsilon_{yy} \\ \varepsilon_{zz} \\ 2\varepsilon_{yz} \\ 2\varepsilon_{xz} \\ 2\varepsilon_{xy} \end{Bmatrix}$$
$$+ \Gamma \begin{bmatrix} \varepsilon_{11} & 0 & 0 \\ 0 & \varepsilon_{22} & 0 \\ 0 & 0 & \varepsilon_{33} \end{bmatrix} \begin{Bmatrix} E_x \\ E_y \\ E_z \end{Bmatrix} + \Gamma \begin{bmatrix} \mathrm{g}_{11} & 0 & 0 \\ 0 & \mathrm{g}_{22} & 0 \\ 0 & 0 & \mathrm{g}_{33} \end{bmatrix} \begin{Bmatrix} H_x \\ H_y \\ H_z \end{Bmatrix} \tag{32b}$$

$$\begin{Bmatrix} \mathcal{L}(B_x) \\ \mathcal{L}(B_y) \\ \mathcal{L}(B_z) \end{Bmatrix} = \Gamma \begin{bmatrix} 0 & 0 & 0 & 0 & q_{15} & 0 \\ 0 & 0 & 0 & q_{24} & 0 & 0 \\ q_{31} & q_{32} & q_{33} & 0 & 0 & 0 \end{bmatrix} \begin{Bmatrix} \varepsilon_{xx} \\ \varepsilon_{yy} \\ \varepsilon_{zz} \\ 2\varepsilon_{yz} \\ 2\varepsilon_{xz} \\ 2\varepsilon_{xy} \end{Bmatrix}$$
$$+ \Gamma \begin{bmatrix} \varepsilon_{11} & 0 & 0 \\ 0 & \varepsilon_{22} & 0 \\ 0 & 0 & \varepsilon_{33} \end{bmatrix} \begin{Bmatrix} E_x \\ E_y \\ E_z \end{Bmatrix} + \Gamma \begin{bmatrix} \mu_{11} & 0 & 0 \\ 0 & \mu_{22} & 0 \\ 0 & 0 & \mu_{33} \end{bmatrix} \begin{Bmatrix} H_x \\ H_y \\ H_z \end{Bmatrix}. \tag{32c}$$

The elements of electric E_i and magnetic loads H_i are defined with three-dimensional electric $\breve{\varphi}$ and magnetic potentials $\breve{\psi}$ as follows (Żur et al. 2020):

$$E_i = \{-\breve{\varphi}_i\},\ H_i = \left\{-\breve{\psi}_{,i}\right\}, \quad i = x, y, z. \tag{33}$$

The electric and magnetic potentials in three dimensions satisfying Maxwell's equations are defined with a cosine function, as given below (Arefi and Zenkour 2018, 2016):

$$\begin{Bmatrix} \breve{\varphi}(x, y, z, t) \\ \breve{\psi}(x, y, z, t) \end{Bmatrix} = \begin{Bmatrix} \varphi_0 \\ \psi_0 \end{Bmatrix} \frac{2\hat{z}}{H_t} - \begin{Bmatrix} \varphi(x, y, t) \\ \psi(x, y, t) \end{Bmatrix} cos\left(\frac{\pi \hat{z}}{H_t}\right), \tag{34}$$

where φ_0 and ψ_0 represent the initial conditions for electric and magnetic charges, respectively; $\varphi(x, y, t)$ and $\psi(x, y, t)$ are the time-dependent electric and magnetic potential distributions, respectively; $\hat{z}$ variable is defined for the upper and lower MEE face layers. $\hat{z}$ is denoted as $\hat{z} = z + h_s/2 + h_r + h_p/2$ for the upper face layer and $\hat{z} = z - h_s/2 - h_r - h_p/2$ for the lower face layer.

2.8 Equations of motion

To get the differential equations of the MEE nanoplate, the virtual displacement approach (Reddy 2020), a variant of the Hamilton method, is applied:

$$\int_0^T (\delta\mathcal{U} - \delta\mathcal{E} - \delta\mathcal{M} - \delta\mathcal{K} + \delta\mathcal{V})\, dt = 0. \tag{35}$$

Here, $\delta\mathcal{U}$, $\delta\mathcal{K}$, and $\delta\mathcal{V}$ represent the virtual strain energy, kinetic energy, and virtual work obtained by applied external forces, respectively. Also, $\delta\mathcal{E}$ and $\delta\mathcal{M}$ define the electric and magnetic energy, respectively. The strain energy, denoted by $\delta\mathcal{U}$, is obtained by

$$\begin{aligned}
\delta\mathcal{U} = \int_\Omega \Bigg[& \int_{h_1}^{h_2} \left(\sigma_{xx}^{lp}\delta\varepsilon_{xx} + \sigma_{yy}^{lp}\delta\varepsilon_{yy} + \sigma_{zz}^{lp}\delta\varepsilon_{zz} + 2\sigma_{yz}^{lp}\delta\varepsilon_{yz} + 2\sigma_{xz}^{lp}\delta\varepsilon_{xz} + 2\sigma_{xy}^{lp}\delta\varepsilon_{xy}\right) dz \\
& + \int_{h_2}^{h_3} \left(\sigma_{xx}^{lr}\delta\varepsilon_{xx} + \sigma_{yy}^{lr}\delta\varepsilon_{yy} + \sigma_{zz}^{lr}\delta\varepsilon_{zz} + 2\sigma_{yz}^{lr}\delta\varepsilon_{yz} + 2\sigma_{xz}^{lr}\delta\varepsilon_{xz} + 2\sigma_{xy}^{lr}\delta\varepsilon_{xy}\right) dz \\
& + \int_{h_3}^{h_4} \left(\sigma_{xx}^{s}\delta\varepsilon_{xx} + \sigma_{yy}^{s}\delta\varepsilon_{yy} + \sigma_{zz}^{s}\delta\varepsilon_{zz} + 2\sigma_{yz}^{s}\delta\varepsilon_{yz} + 2\sigma_{xz}^{s}\delta\varepsilon_{xz} + 2\sigma_{xy}^{s}\delta\varepsilon_{xy}\right) dz \\
& + \int_{h_4}^{h_5} \left(\sigma_{xx}^{ur}\delta\varepsilon_{xx} + \sigma_{yy}^{ur}\delta\varepsilon_{yy} + \sigma_{zz}^{ur}\delta\varepsilon_{zz} + 2\sigma_{yz}^{ur}\delta\varepsilon_{yz} + 2\sigma_{xz}^{ur}\delta\varepsilon_{xz} + 2\sigma_{xy}^{ur}\delta\varepsilon_{xy}\right) dz \\
& + \int_{h_5}^{h_6} \Big(\Big(\sigma_{xx}^{up}\delta\varepsilon_{xx} + \sigma_{yy}^{up}\delta\varepsilon_{yy} + \sigma_{zz}^{up}\delta\varepsilon_{zz} + 2\sigma_{yz}^{up}\delta\varepsilon_{yz} \\
& + 2\sigma_{xz}^{up}\delta\varepsilon_{xz} + 2\sigma_{xy}^{up}\delta\varepsilon_{xy}\Big) dz\Big)\Bigg] dxdy.
\end{aligned} \tag{36}$$

The electric $\delta\mathcal{E}$ and magnetic $\delta\mathcal{M}$ energy contributions can be defined by

$$\begin{aligned}
\delta\mathcal{E} = \int_\Omega \Bigg[& \int_{h_1}^{h_2} \left(D_x\delta E_x + D_y\delta E_{y+} D_z\delta E_z\right) dz \\
& + \int_{h_5}^{h_6} \left(D_x\delta E_x + D_y\delta E_{y+} D_z\delta E_z\right) dz \Bigg] dxdy,
\end{aligned} \tag{37}$$

$$\begin{aligned}
\delta\mathcal{M} = \int_\Omega \Bigg[& \int_{h_1}^{h_2} \left(B_x\delta H_x + B_y\delta H_{y+} B_z\delta H_z\right) dz \\
& + \int_{h_5}^{h_6} \left(B_x\delta H_x + B_y\delta H_{y+} B_z\delta H_z\right) dz \Bigg] dxdy.
\end{aligned} \tag{38}$$

Additionally, the kinetic energy is given by

$$\begin{aligned}\delta\mathcal{K} = \int_{\Omega}\Bigg[&\int_{h_1}^{h_2}\rho^{lp}\left(\dot{u}\delta\dot{u}+\dot{v}\delta\dot{v}+\dot{w}\delta\dot{w}\right)dz+\int_{h_2}^{h_3}\rho^{lr}\left(z\right)\left(\dot{u}\delta\dot{u}+\dot{v}\delta\dot{v}+\dot{w}\delta\dot{w}\right)dz\\&+\int_{h_3}^{h_4}\rho^{s}\left(z\right)\left(\dot{u}\delta\dot{u}+\dot{v}\delta\dot{v}+\dot{w}\delta\dot{w}\right)dz+\int_{h_4}^{h_5}\rho^{ur}\left(z\right)\left(\dot{u}\delta\dot{u}+\dot{v}\delta\dot{v}+\dot{w}\delta\dot{w}\right)dz\\&+\int_{h_5}^{h_6}\rho^{up}\left(\dot{u}\delta\dot{u}+\dot{v}\delta\dot{v}+\dot{w}\delta\dot{w}\right)\Bigg]dxdy,\end{aligned}\tag{39}$$

where $\rho^{p}(z)$, $\rho^{s}(z)$, and $\rho^{r}(z)$ are the densities of the piezomagnetic face layers, auxetic core layer, and rim layers, respectively. The virtual work can be calculated by

$$\begin{aligned}\delta\mathcal{V} = -\int_{\Omega}\Bigg[&\left(N_{xx0}+N_{xx\mathcal{E}}+N_{xx\mathcal{M}}\right)\frac{\partial w_b}{\partial x}\frac{\partial\delta w_b}{\partial x}\\&+\left(N_{yy0+}N_{yy\mathcal{E}}+N_{xx\mathcal{M}}\right)\frac{\partial w_b}{\partial y}\frac{\partial\delta w_b}{\partial y}+\Bigg]dxdy,\end{aligned}\tag{40}$$

where, the 0, $\mathcal{E}$, and $\mathcal{M}$ subscripts define the compressive mechanical, electrical, and magnetic forces, respectively. The following equation represents the thickness-integrated resultant forces and moments:

$$\begin{aligned}&\begin{Bmatrix}N_{xx} & N_{yy} & N_{xy}\\ M_{xx}^{(b)} & M_{yy}^{(b)} & M_{xy}^{(b)}\\ M_{xx}^{(s)} & M_{yy}^{(s)} & M_{xy}^{(s)}\end{Bmatrix}\\&=\int_{h_1}^{h_2}\left(\sigma_{xx}^{lp},\sigma_{yy}^{lp},\sigma_{xy}^{lp}\right)\begin{Bmatrix}1\\ z\\ f\left(z\right)\end{Bmatrix}dz+\int_{h_2}^{h_3}\left(\sigma_{xx}^{lr},\sigma_{yy}^{lr},\sigma_{xy}^{lr}\right)\begin{Bmatrix}1\\ z\\ f\left(z\right)\end{Bmatrix}dz\\&+\int_{h_3}^{h_4}\left(\sigma_{xx}^{s},\sigma_{yy}^{s},\sigma_{xy}^{s}\right)\begin{Bmatrix}1\\ z\\ f\left(z\right)\end{Bmatrix}dz+\int_{h_4}^{h_5}\left(\sigma_{xx}^{ur},\sigma_{yy}^{ur},\sigma_{xy}^{ur}\right)\begin{Bmatrix}1\\ z\\ f\left(z\right)\end{Bmatrix}dz\\&+\int_{h_5}^{h_6}\left(\sigma_{xx}^{up},\sigma_{yy}^{up},\sigma_{xy}^{up}\right)\begin{Bmatrix}1\\ z\\ f\left(z\right)\end{Bmatrix}dz,\end{aligned}\tag{41a}$$

$$\begin{aligned}N_{zz} = &\int_{h_1}^{h_2}\sigma_{zz}^{lp}g'(z)dz+\int_{h_2}^{h_3}\sigma_{zz}^{lr}g'(z)dz+\int_{h_3}^{h_4}\sigma_{zz}^{s}g'(z)dz\\&+\int_{h_4}^{h_5}\sigma_{zz}^{ur}g'(z)dz+\int_{h_5}^{h_6}\sigma_{zz}^{up}g'\left(z\right)dz,\end{aligned}\tag{41b}$$

$$\begin{aligned}\left\{S_{xz},S_{yz}\right\} = &\int_{h_1}^{h_2}\left\{\sigma_{xz}^{lp},\sigma_{yz}^{lp}\right\}\mathrm{g}\left(z\right)dz+\int_{h_2}^{h_3}\left\{\sigma_{xz}^{lr},\sigma_{yz}^{lr}\right\}\mathrm{g}\left(z\right)dz\\&+\int_{h_3}^{h_4}\left\{\sigma_{xz}^{s},\sigma_{yz}^{s}\right\}\mathrm{g}\left(z\right)dz+\int_{h_4}^{h_5}\left\{\sigma_{xz}^{ur},\sigma_{yz}^{ur}\right\}\mathrm{g}\left(z\right)dz\\&+\int_{h_5}^{h_6}\left\{\sigma_{xz}^{up},\sigma_{yz}^{up}\right\}\mathrm{g}\left(z\right)dz.\end{aligned}\tag{41c}$$

Additionally, the strain energy can be rearranged as follows:

$$\begin{aligned}\delta\mathcal{U} = \int_{\Omega} \big(& N_{xx}\delta\varepsilon_{xx}^{(0)} + N_{yy}\delta\varepsilon_{yy}^{(0)} + N_{zz}\delta\varepsilon_{zz}^{(0)} + N_{xy}\delta\varepsilon_{xy}^{(0)} + N_{xz}\delta\varepsilon_{xz}^{(0)} \\ & + N_{yz}\delta\varepsilon_{yz}^{(0)} + M_{xx}\delta\varepsilon_{xx}^{(b)} + M_{yy}\delta\varepsilon_{yy}^{(b)} + M_{xy}\delta\varepsilon_{xy}^{(b)} + M_{xx}\delta\varepsilon_{xx}^{(b)} \\ & + M_{yy}\delta\varepsilon_{yy}^{(b)} + M_{xy}\delta\varepsilon_{xy}^{(b)} \big)\, dxdy.\end{aligned} \tag{42}$$

The thickness-related electric and magnetic constants are defined as follows:

$$\begin{aligned}\left\{\overline{D}_x, \overline{D}_y, \overline{D}_z\right\} = & \int_{h_1}^{h_2} \left(D_x, D_y, D_z\right) \begin{Bmatrix} cos\left(\frac{\pi z_2}{h_{lp}}\right) \\ cos\left(\frac{\pi z_2}{h_{lp}}\right) \\ \frac{\pi}{h_{lp}} sin\left(\frac{\pi z_2}{h_{lp}}\right) \end{Bmatrix} dz \\ & + \int_{h_5}^{h_6} \left(D_x, D_y, D_z\right) \begin{Bmatrix} cos\left(\frac{\pi z_1}{h_{up}}\right) \\ cos\left(\frac{\pi z_1}{h_{up}}\right) \\ \frac{\pi}{h_{up}} sin\left(\frac{\pi z_1}{h_{up}}\right) \end{Bmatrix} dz,\end{aligned} \tag{43a}$$

$$\begin{aligned}\left\{\overline{B}_x, \overline{B}_y, \overline{B}_z\right\} = & \int_{h_1}^{h_2} \left(B_x, B_y, B_z\right) \begin{Bmatrix} cos\left(\frac{\pi z_2}{h_{lp}}\right) \\ cos\left(\frac{\pi z_2}{h_{lp}}\right) \\ \frac{\pi}{h_{lp}} sin\left(\frac{\pi z_2}{h_{lp}}\right) \end{Bmatrix} dz \\ & + \int_{h_5}^{h_6} \left(B_x, B_y, B_z\right) \begin{Bmatrix} cos\left(\frac{\pi z_1}{h_{up}}\right) \\ cos\left(\frac{\pi z_1}{h_{up}}\right) \\ \frac{\pi}{h_{up}} sin\left(\frac{\pi z_1}{h_{up}}\right) \end{Bmatrix} dz.\end{aligned} \tag{43b}$$

The virtual form of electric and magnetic loads may be rearranged as follows:

$$\delta\mathcal{E} = \int_{\Omega} \left(\overline{D}_x \frac{\partial\delta\varphi}{\partial x} + \overline{D}_y \frac{\partial\delta\varphi}{\partial y} - \overline{D}_z \delta\varphi \right) dxdy, \tag{44}$$

$$\delta\mathcal{M} = \int_{\Omega} \left(\overline{B}_x \frac{\partial\delta\psi}{\partial x} + \overline{B}_y \frac{\partial\delta\psi}{\partial y} - \overline{B}_z \delta\psi \right) dxdy. \tag{45}$$

The virtual kinetic energy mass inertia can be defined as

$$\begin{aligned}\delta\mathcal{K} = \int_{\Omega} [& m_0 \left(\dot{u}_0\delta\dot{u}_0 + \dot{v}_0\delta\dot{v}_0 + \dot{w}_b\delta\dot{w}_b + \dot{w}_b\delta\dot{w}_s + \dot{w}_s\delta\dot{w}_0 + \dot{w}_s\delta\dot{w}_s\right) \\ & - m_1 \left(\dot{u}_0 \frac{\partial\delta\dot{w}_b}{dx} + \frac{\partial\dot{w}_b}{dx}\delta\dot{u}_0 + \dot{v}_0 \frac{\partial\delta\dot{w}_b}{dy} + \frac{\partial\dot{w}_b}{dy}\delta\dot{v}_0 \right) \\ & - m_2 \left(\frac{\partial\dot{w}_b}{dx}\frac{\partial\delta\dot{w}_b}{dx} + \frac{\partial\dot{w}_b}{dy}\frac{\partial\delta\dot{w}_b}{dy} \right) \\ & - m_3 \left(\dot{u}_0 \frac{\partial\delta\dot{w}_b}{dx} + \frac{\partial\dot{w}_b}{dx}\delta\dot{u}_0 + \dot{v}_0 \frac{\partial\delta\dot{w}_b}{dy} + \frac{\partial\dot{w}_b}{dy}\delta\dot{v}_0 \right)\end{aligned} \tag{46}$$

$$
\begin{aligned}
&+ m_4 \left(\frac{\partial \dot{w}_b}{dx} \frac{\partial \delta \dot{w}_b}{dx} + \frac{\partial \dot{w}_b}{dx} \frac{\partial \delta \dot{w}_b}{dx} + \frac{\partial \dot{w}_b}{dy} \frac{\partial \delta \dot{w}_b}{dy} + \frac{\partial \dot{w}_b}{dy} \frac{\partial \delta \dot{w}_b}{dy} \right) \\
&+ m_5 \left(\frac{\partial \dot{w}_s}{dx} \frac{\partial \delta \dot{w}_s}{dx} + \frac{\partial \dot{w}_s}{dy} \frac{\partial \delta \dot{w}_s}{dy} \right) + m_6 \left(\dot{w}_b \delta \dot{\phi} + \dot{w}_s \delta \dot{\phi} + \dot{\phi} \delta \dot{w}_b + \dot{\phi} \delta \dot{w}_s \right) \\
&+ m_7 \dot{\phi} \delta \dot{\phi} \Big] dx dy,
\end{aligned}
$$

in which

$$
\begin{aligned}
m_i = &\int_{h_1}^{h_2} \rho^{lp} z^i dz + \int_{h_2}^{h_3} p^{lr}(z) z^i dz + \int_{h_3}^{h_4} p^s(z) z^i dz \\
&+ \int_{h_4}^{h_5} p^{ur}(z) z^i dz + \int_{h_5}^{h_6} \rho^{up} z^i dz,
\end{aligned} \tag{47a}
$$

$$
\begin{aligned}
m_{i+3} = &\int_{h_1}^{h_2} \rho^{lp} f(z) z^i dz + \int_{h_2}^{h_3} p^{lr}(z) f(z) z^i dz \\
&+ \int_{h_3}^{h_4} p^s(z) f(z) z^i dz + \int_{h_4}^{h_5} p^{ur}(z) f(z) z^i dz + \int_{h_5}^{h_6} \rho^{up} f(z) z^i dz,
\end{aligned} \tag{47b}
$$

$$
\begin{aligned}
m_6 = &\int_{h_1}^{h_2} \rho^{lp} \mathrm{g}(z) dz + \int_{h_2}^{h_3} p^{lr}(z) \mathrm{g}(z) dz \\
&+ \int_{h_3}^{h_4} p^s(z) \mathrm{g}(z) dz + \int_{h_4}^{h_5} p^{ur}(z) \mathrm{g}(z) dz + \int_{h_5}^{h_6} \rho^{up} \mathrm{g}(z) dz,
\end{aligned} \tag{47c}
$$

$$
\begin{aligned}
m_7 = &\int_{h_1}^{h_2} \rho^{lp} \mathrm{g}^2(z) dz + \int_{h_2}^{h_3} p^{lr}(z) \mathrm{g}^2(z) dz \\
&+ \int_{h_3}^{h_4} p^s(z) \mathrm{g}^2(z) dz + \int_{h_4}^{h_5} p^{ur}(z) \mathrm{g}^2(z) dz + + \int_{h_5}^{h_6} \rho^{up} \mathrm{g}^2(z) dz,
\end{aligned} \tag{47d}
$$

where $i = 0, 1, 2$. In its final form, the virtual information resulting from applied external forces is presented by

$$
\delta \mathcal{V} = \int_{\Omega} \left[\left(p_{x0} + p_{e31} + p_{q31} \right) \frac{\partial w_b}{\partial x} \frac{\partial \delta w_b}{\partial x} + \left(p_{y0} \right) + p_{e32} + p_{q32}) \frac{\partial w_b}{\partial x} \frac{\partial \delta w_b}{\partial x} \right] dx dy. \tag{48}
$$

The mechanical compression forces are assumed to be equal to $p_{x0} = N_0$ and $p_{y0} = \gamma N_0$. The electric force p_{e3i} and the magnetic force p_{q3i} are expressed as

$$
p_{e3i} = - \left[\int_{h_1}^{h_2} e_{3i} \left(\frac{2V_0}{h_{lp}} \right) dz + \int_{h_2}^{h_3} e_{3i}(z) \left(\frac{2V_0}{h_s} \right) dz + \int_{h_3}^{h_4} e_{3i} \frac{2V_0}{h_{up}} dz \right], \tag{49a}
$$

$$
p_{q3i} = - \left[\int_{h_1}^{h_2} q_{3i} \left(\frac{2H_0}{h_{lp}} \right) dz + \int_{h_2}^{h_3} q_{3i}(z) \left(\frac{2H_0}{h_s} \right) dz + \int_{h_3}^{h_4} q_{3i} \left(\frac{2H_0}{h_{up}} \right) dz \right], \tag{49b}
$$

where $i = 1,\ 2$. Due to the temperature rise, the thermomechanical loads N_x^T and N_y^T in the x-y directions are given by

$$N_x^T = b\left[\int_{h_1}^{h_2} C_{11}^p \alpha_{lp} \Delta T dz + \int_{h_2}^{h_3} C_{11}^{lr} \alpha_{lr} \Delta T dz + \int_{h_3}^{h_4} C_{11}^s \alpha_s \Delta T dz + \int_{h_4}^{h_5} C_{11}^{ur} \alpha_{ur} \Delta T dz + \int_{h_5}^{h_6} C_{11}^p \alpha_{up} \Delta T dz\right], \tag{50a}$$

$$N_y^T = a\left[\int_{h_1}^{h_2} C_{11}^p \alpha_{lp} \Delta T dz + \int_{h_2}^{h_3} C_{11}^{lr} \alpha_{lr} \Delta T dz + \int_{h_3}^{h_4} C_{11}^s \alpha_s \Delta T dz + \int_{h_4}^{h_5} C_{11}^{ur} \alpha_{ur} \Delta T dz + \int_{h_5}^{h_6} C_{11}^p \alpha_{up} \Delta T dz\right]. \tag{50b}$$

Differential equations representing the motion of the sandwich nanoplate can be obtained by substituting the virtual energy contributions $\delta\mathcal{U}$, $\delta\mathcal{E}$, $\delta\mathcal{M}$, $\delta\mathcal{K}$, and $\delta\mathcal{V}$ from Eqs. (42), (44–46), and (48) into Eq. (35).

$$\delta u_0 : \frac{\partial N_{xx}}{\partial x} + \frac{\partial N_{xy}}{\partial x} = m_0 \ddot{u}_0 - m_1 \frac{\partial \ddot{w}_b}{\partial x} - m_1 \frac{\partial \ddot{w}_s}{\partial x} \tag{51a}$$

$$\delta v_0 : \frac{\partial N_{yy}}{\partial y} + \frac{\partial N_{xy}}{\partial x} = m_0 \ddot{v}_0 - m_1 \frac{\partial \ddot{w}_b}{\partial y} - m_3 \frac{\partial \ddot{w}_s}{\partial y} \tag{51b}$$

$$\begin{aligned} \delta w_b : & \frac{\partial^2 M_{xx}^{(b)}}{\partial x^2} + 2\frac{\partial^2 M_{xy}^{(b)}}{dxdy} + \frac{\partial^2 M_{yy}^{(b)}}{dy^2} - \left(N_x^T + p_{x0} + p_{e31} + p_{q31}\right)\frac{\partial^2 w_b}{\partial x^2} \\ & - \left(N_y^T + p_{x0} + p_{e31} + p_{q31}\right)\frac{\partial^2 w_b}{\partial y^2} \\ = & m_0\left(\ddot{w}_b + \ddot{w}_s\right) + m_1\left(\frac{\partial \ddot{u}_0}{\partial x} + \frac{\partial \ddot{v}_0}{\partial y}\right) - m_2\left(\frac{\partial \ddot{w}_b}{\partial x^2} + \frac{\partial \ddot{w}_b}{\partial y^2}\right) \\ & - m_4\left(\frac{\partial^2 \ddot{w}_s}{dx^2} + \frac{\partial^2 \ddot{w}_s}{dy^2}\right) + m_6\ddot{\phi} \end{aligned} \tag{51c}$$

$$\begin{aligned} \delta w_s : & \frac{\partial^2 M_{xx}^{(s)}}{\partial x^2} + 2\frac{\partial^2 M_{xy}^{(s)}}{dxdy} + \frac{\partial^2 M_{yy}^{(s)}}{dy^2} + \frac{\partial S_{xz}}{\partial x} + \frac{\partial S_{yz}}{\partial y} \\ = & m_0\left(\ddot{w}_b + \ddot{w}_s\right) + m_3\left(\frac{\partial \ddot{u}_0}{\partial x} + \frac{\partial \ddot{v}_0}{\partial y}\right) - m_4\left(\frac{\partial^2 \ddot{w}_b}{dx^2} + \frac{\partial^2 \ddot{w}_b}{dy^2}\right) \\ & - m_5\left(\frac{\partial^2 \ddot{w}_s}{dx^2} + \frac{\partial^2 \ddot{w}_s}{dy^2}\right) + m_6\ddot{\phi} \end{aligned} \tag{51d}$$

$$\delta\phi : \frac{\partial S_{xz}}{\partial x} + \frac{\partial S_{yz}}{\partial y} - N_{zz} = m_6\left(\ddot{w}_b + \ddot{w}_s\right) + m_7\ddot{\phi} \tag{51e}$$

$$\delta\varphi : \frac{\partial \overline{D}_x}{\partial x} + \frac{\partial \overline{D}_{YZ}}{\partial y} + \overline{D}_z = 0 \tag{51f}$$

$$\delta\psi : \frac{\partial \overline{B}_x}{\partial x} + \frac{\partial \overline{B}_{yz}}{\partial y} + \overline{B}_z = 0. \tag{51g}$$

The boundary conditions of the sandwich nanoplate are given as

$$\delta u_0 : 0 = N_{xx} n_x + N_{xy} n_y - m_1 \ddot{w}_b n_x - m_3 \ddot{w}_s n_x \tag{52a}$$

$$\delta v_0 : 0 = N_{yy} n_y + N_{xy} n_x - m_1 \ddot{w}_b n_y - m_3 \ddot{w}_s n_y \tag{52b}$$

$$\begin{aligned} \delta w_b : 0 = & \left[\frac{\partial M_{xx}^{(b)}}{\partial x} + \frac{\partial M_{xy}^{(b)}}{\partial y} - \left(N_x^T + p_{x0} + p_{e31} + p_{q31} \right) \frac{\partial w_b}{\partial x} \right] n_x \\ & + \left[\frac{\partial M_{yy}^{(b)}}{\partial y} + \frac{\partial M_{xy}^{(b)}}{\partial x} \frac{\partial M_{xy}^{(b)}}{\partial y} - \left(N_y^T + p_{y0} + p_{e32} + p_{q32} \right) \frac{\partial w_b}{\partial y} \right] n_y \\ & + \left(m_1 \ddot{u}_0 - m_2 \frac{\partial \ddot{w}_b}{\partial x} - m_4 \frac{\partial \ddot{w}_s}{\partial x} \right) n_x + \left(m_1 \ddot{v}_0 - m_2 \frac{\partial \ddot{w}_b}{\partial y} - m_4 \frac{\partial \ddot{w}_s}{\partial y} \right) n_y \end{aligned} \tag{52c}$$

$$\delta \frac{\partial w_b}{\partial n} : 0 = M_{nn}^{(b)} \tag{52d}$$

$$\delta \frac{\partial w_s}{\partial n} : 0 = M_{nn}^{(s)} \tag{52e}$$

$$\delta\phi : 0 = S_{xz} n_x + S_{yz} n_y \tag{52f}$$

$$\delta\varphi : 0 = \overline{D}_x n_x + \overline{D}_y n_y, \tag{52g}$$

where

$$M_{nn}^{(b)} = M_{xx}^{(b)} n_x^2 + 2M_{xy}^{(b)} n_x n_y + M_{yy}^{(b)} n_y^2, \; M_{nn}^{(s)} = M_{xx}^{(s)} n_x^2 + 2M_{xy}^{(s)} n_x n_y + M_{yy}^{(s)} n_x^2. \tag{53}$$

The equilibrium equations for the displacements and MEE coefficients of a nanostructure may be calculated as follows by combining the nonlocal and strain-gradient differential operators $\mathcal{L}(*) \equiv 1 - (e_0 a)^2 \nabla^2$ and $\Gamma(*) \equiv 1 - (l_m)^2 \nabla^2$:

$$\begin{aligned} & \Gamma \left[A_{11}^{(0)} \frac{\partial^2 u_0}{\partial x^2} - A_{11}^{(1)} \frac{\partial^3 w_b}{\partial x^3} - A_{11}^{-(0)} \frac{\partial^3 w_s}{\partial x^3} + \left(A_{12}^{(0)} + A_{66}^{(0)} \right) \frac{\partial v_0}{\partial x \partial y} \right. \\ & \quad - \left(A_{12}^{(1)} + 2A_{66}^{(1)} \right) \frac{\partial^3 w_s}{\partial x \partial y^2} - \left(A_{12}^{-(0)} + 2A_{66}^{-(0)} \right) \frac{\partial^3 w_s}{\partial x \partial y^2} + A_{66}^{(0)} \frac{\partial^2 u_0}{\partial y^2} \\ & \quad \left. + \tilde{A}_{13}^{(0)} \frac{\partial \phi}{\partial x} + \overline{B}_{e31}^{(0)} \frac{\partial \varphi}{\partial x} + \overline{B}_{q31}^{(0)} \frac{\partial \psi}{\partial x} \right] \\ & = \mathcal{L} \left[m_0 \ddot{u}_0 - m_1 \frac{\partial \ddot{w}_b}{\partial x} - m_3 \frac{\partial \ddot{w}_s}{\partial x} \right] \end{aligned} \tag{54a}$$

$$\begin{aligned} & \Gamma \left[A_{22}^{(0)} \frac{\partial^2 v_0}{\partial y^2} - A_{22}^{(1)} \frac{\partial^3 w_b}{\partial y^3} - A_{22}^{-(0)} \frac{\partial^3 w_s}{\partial y^3} + \left(A_{12}^{(0)} + A_{66}^{(0)} \right) \frac{\partial u_0}{\partial x \partial y} \right. \\ & \quad - \left(A_{12}^{(1)} + 2A_{66}^{(1)} \right) \frac{\partial^3 w_b}{\partial x^2 \partial y} - \left(A_{12}^{-(0)} + 2A_{66}^{-(0)} \right) \frac{\partial^3 w_s}{\partial x^2 \partial y} + A_{66}^{(0)} \frac{\partial^2 v_0}{\partial x^2} \\ & \quad \left. + \tilde{A}_{13}^{(0)} \frac{\partial \phi}{\partial y} + \overline{B}_{e32}^{(0)} \frac{\partial \varphi}{\partial y} + \overline{B}_{e32}^{(0)} \frac{\partial \psi}{\partial y} \right] = \mathcal{L} \left[m_0 \ddot{v}_0 - m_1 \frac{\partial \ddot{w}_b}{\partial y} - m_3 \frac{\partial \ddot{w}_s}{\partial y} \right] \end{aligned} \tag{54b}$$

$$\Gamma\Bigg[A_{11}^{(1)}\frac{\partial^3 u_0}{\partial x^3}-A_{22}^{(2)}\frac{\partial^4 w_b}{\partial y^4}-A_{11}^{-(1)}\frac{\partial^4 w_s}{\partial y^4}+\left(A_{12}^{(1)}+2A_{66}^{(1)}\right)\left(\frac{\partial^3 u_0}{\partial x\partial y^2}+\frac{\partial^3 v_0}{\partial x^2\partial y}\right)$$
$$-2\left(A_{12}^{(2)}+2A_{66}^{(2)}\right)\frac{\partial^4 w_b}{\partial x^2\partial y^2}-2\left(A_{12}^{-(1)}+2A_{66}^{-(1)}\right)\frac{\partial^4 w_s}{\partial x^2\partial y^4}$$
$$+A_{22}^{(1)}\frac{\partial^3 v_0}{\partial x^3}-A_{22}^{(2)}\frac{\partial^4 w_b}{\partial y^4}-\overline{A}_{22}^{(1)}\frac{\partial^4 w_s}{\partial y^4}+\tilde{A}_{13}^{(1)}\frac{\partial^2\phi}{\partial x^2}+A_{23}^{(1)}\frac{\partial^2\phi}{\partial y^2}$$
$$+\overline{B}_{e31}^{(1)}\frac{\partial^2\varphi}{\partial x^2}+\overline{B}_{e32}^{(1)}\frac{\partial^2\varphi}{\partial y^2}+\overline{B}_{q31}^{(1)}\frac{\partial^2\psi}{\partial x^2}+\overline{B}_{q32}^{(1)}\frac{\partial^2\psi}{\partial y^2}\Bigg] \tag{54c}$$
$$=\mathcal{L}\Bigg[\left(N_x^T+P_{x0}+P_{e31}+P_{q31}\right)\frac{\partial^2 w_b}{\partial x^2}+\left(N_y^T+P_{y0}+P_{e32}+P_{q32}\right)\frac{\partial^2 w_b}{\partial y^2}$$
$$+m_0\left(\ddot{w}_b+\ddot{w}_s\right)+m_1\left(\frac{\partial\ddot{u}_0}{\partial x}+\frac{\partial\ddot{u}_0}{\partial y}\right)-m_2\left(\frac{\partial^2\ddot{w}_b}{\partial x^2}+\frac{\partial^2\ddot{w}_b}{\partial y^2}\right)$$
$$-m_4\left(\frac{\partial^2\ddot{w}_b}{\partial x^2}+\frac{\partial^2\ddot{w}_b}{\partial y^2}\right)+m_6\ddot{\phi}\Bigg]$$

$$\Gamma\Bigg[\overline{A}_{11}^{(0)}\frac{\partial^3 u_0}{\partial x^3}-\overline{A}_{11}^{(1)}\frac{\partial^4 w_b}{\partial x^4}-\overline{A}_{11}^{(f)}\frac{\partial^4 w_s}{\partial x^4}+\left(\overline{A}_{12}^{(0)}+2\overline{A}_{66}^{(0)}\right)\left(\frac{\partial^3 u_0}{\partial x\partial y^2}+\frac{\partial^3 v_0}{\partial x^2\partial y}\right)$$
$$-2\left(\overline{A}_{12}^{(1)}+2\overline{A}_{66}^{(1)}\right)\frac{\partial^4 w_b}{\partial x^2\partial y^2}-2\left(\overline{A}_{12}^{(f)}+2\overline{A}_{66}^{(f)}\right)\frac{\partial^4 w_s}{\partial x^2\partial y^2}+\overline{A}_{22}^{(0)}\frac{\partial^3 v_0}{\partial y^3}$$
$$-\overline{A}_{22}^{(1)}\frac{\partial^4 w_b}{\partial y^4}-\overline{A}_{22}^{(f)}\frac{\partial^4 w_s}{\partial y^4}+\hat{A}_{44}^{(0)}\frac{\partial^2 w_s}{\partial y^2}+\hat{A}_{55}^{(0)}\frac{\partial^2 w_s}{\partial x^2}+\left(\tilde{A}_{13}^{(f)}+\hat{A}_{55}^{(0)}\right)\frac{\partial^2\phi}{\partial x^2}$$
$$+\left(\tilde{A}_{23}^{(f)}+\hat{A}_{44}^{(0)}\right)\frac{\partial^2\phi}{\partial y^2}+\left(B_{e31}^{(f)}-B_{e15}^{(g)}\right)\frac{\partial^2\varphi}{\partial x^2}++\ddot{w}_s)+m_3\left(\frac{\partial\ddot{u}_0}{\partial x}+\frac{\partial\ddot{v}_0}{\partial y}\right) \tag{54d}$$
$$-m_4(\frac{\partial^2\ddot{w}_0}{\partial x^2}\left(\overline{B}_{e32}^{(f)}-B_{e24}^{(g)}\right)\frac{\partial^2\varphi}{\partial y^2}+\left(\overline{B}_{q31}^{(f)}-B_{q15}^{(g)}\right)\frac{\partial^2\psi}{\partial x^2}\Bigg]$$
$$=\mathcal{L}\Bigg[\left(N_x^T+P_{x0}+P_{e31}+P_{q31}\right)\frac{\partial^2 w_b}{\partial x^2}+\left(N_y^T+P_{y0}+P_{e32}+P_{q32}\right)\frac{\partial^2 w_b}{\partial y^2}$$
$$+\left(m_0\left(\ddot{w}_0+\frac{\partial^2\ddot{w}_b}{\partial y^2}\right)\right)-m_5\left(\frac{\partial^2\ddot{w}_s}{\partial x^2}+\frac{\partial^2\ddot{w}_s}{\partial y^2}\right)+m_6\ddot{\phi}\Bigg]$$

$$\Gamma\Bigg[-\tilde{A}_{13}^{(0)}\frac{\partial u_0}{\partial x}+\tilde{A}_{13}^{(1)}\frac{\partial^2 w_b}{\partial x^2}+\left(-\tilde{A}_{13}^{(f)}+\hat{A}_{55}^{(0)}\right)\frac{\partial^2 w_s}{\partial x^2}-\tilde{A}_{23}^{(0)}\frac{\partial v_0}{\partial y}+\tilde{A}_{23}^{(1)}\frac{\partial^2 w_b}{\partial y^2}$$
$$+\left(-\tilde{A}_{23}^{(f)}+\hat{A}_{44}^{(0)}\right)\frac{\partial^2 w_s}{\partial y^2}-\tilde{A}_{33}^{(g)}\phi+\hat{A}_{44}^{(0)}\frac{\partial^2\phi}{\partial y^2}+\hat{A}_{55}^{(0)}\frac{\partial^2\phi}{\partial x^2}-B_{e15}^{(g)}\frac{\partial^2\varphi}{\partial x^2}$$
$$-B_{e24}^{(g)}\frac{\partial^2\varphi}{\partial y^2}-B_{q15}^{(g)}\frac{\partial^2\psi}{\partial x^2}-B_{q24}^{(g)}\frac{\partial^2\psi}{\partial y^2}-\overline{B}_{e33}^{(g)}\varphi-\overline{B}_{q33}^{(g)}\psi+\overline{B}_{e33}^{(g)}+\overline{B}_{q33}^{(g)}\Bigg]$$
$$=\mathcal{L}\left[m_6\left(\ddot{w}_b+\ddot{w}_s\right)+m_7\ddot{\phi}\right]-\tilde{A}_{13}^{(0)}\frac{\partial u_0}{\partial x}+\tilde{A}_{13}^{(1)}\frac{\partial^2 w_b}{\partial x^2}+\left(\tilde{A}_{13}^{(f)}+\hat{A}_{55}^{(0)}\right)\frac{\partial^2 w_b}{\partial x^2} \tag{54e}$$
$$-\tilde{A}_{23}^{(0)}\frac{\partial v_0}{\partial y}+\tilde{A}_{23}^{(1)}\frac{\partial^2 w_b}{\partial y^2}+\left(\tilde{A}_{23}^{(f)}+\hat{A}_{44}^{(0)}\right)\frac{\partial^2 w_s}{\partial y^2}-\left(-\tilde{A}_{23}^{(f)}+\hat{A}_{44}^{(0)}\right)\frac{\partial^2 w_s}{\partial y^2}$$

$$-\tilde{A}_{23}^{(g)}\phi+\hat{A}_{44}^{(0)}\frac{\partial^2\phi}{\partial y^2}+\hat{A}_{55}^{(0)}\frac{\partial^2\phi}{\partial x^2}-B_{e15}^{(g)}\frac{\partial^2\varphi}{\partial x^2}-B_{e24}^{(g)}\frac{\partial^2\varphi}{\partial y^2}-B_{q15}^{(g)}\frac{\partial^2\psi}{\partial x^2}$$
$$-B_{q24}^{(g)}\frac{\partial^2\psi}{\partial y^2}-\overline{B}_{e33}^{(g)}\varphi-\overline{B}_{q33}^{(g)}\psi+B_{e33}^{(1)}+B_{q33}^{(1)}=\mathcal{L}\left[m_6\left(\ddot{w}_b+\ddot{w}_s\right)+m_7\ddot{\phi}\right]$$

$$\begin{aligned}&\overline{B}_{e31}^{(0)}\frac{\partial u_0}{\partial x}+\overline{B}_{e32}^{(0)}\frac{\partial v_0}{\partial y}-\overline{B}_{e31}^{(1)}\frac{\partial^2 w_b}{\partial x^2}-\overline{B}_{e32}^{(1)}\frac{\partial^2 w_b}{\partial y^2}+\left(B_{e15}^{(g)}-\overline{B}_{e31}^{(f)}\right)\frac{\partial^2 w_s}{\partial y^2}\\&+\overline{B}_{e32}^{(g)}\phi+B_{e15}^{(g)}\frac{\partial^2\phi}{\partial x^2}+B_{e24}^{(g)}\frac{\partial^2\phi}{\partial y^2}-P_{\varepsilon33}^{(s2)}\varphi-P_{g33}^{(c2)}\psi+P_{\varepsilon11}^{(c2)}\frac{\partial^2\varphi}{\partial x^2}\\&+P_{\varepsilon22}^{(c2)}\frac{\partial^2\varphi}{\partial y^2}+P_{g11}^{(c2)}\frac{\partial^2\psi}{\partial x^2}+P_{g22}^{(c2)}\frac{\partial^2\psi}{\partial y^2}-P_{g33}^{(s)}-P_{\varepsilon33}^{(s)}=0\end{aligned}\tag{54f}$$

$$\begin{aligned}&\overline{B}_{q31}^{(0)}\frac{\partial u_0}{\partial x}+\overline{B}_{q32}^{(0)}\frac{\partial v_0}{\partial y}-\overline{B}_{q31}^{(1)}\frac{\partial^2 w_b}{\partial x^2}-\overline{B}_{q32}^{(1)}\frac{\partial^2 w_b}{\partial y^2}+\left(B_{q15}^{(g)}-\overline{B}_{q31}^{(f)}\right)\frac{\partial^2 w_s}{\partial x^2}\\&+\left(B_{q24}^{(g)}-\overline{B}_{q32}^{(f)}\right)\frac{\partial^2 w_s}{\partial y^2}+\overline{B}_{q33}^{(g)}\phi+B_{q15}^{(g)}\frac{\partial^2\phi}{\partial x^2}+B_{q24}^{(g)}\frac{\partial^2\phi}{\partial y^2}-P_{g33}^{(s2)}\varphi-P_{\mu33}^{(c2)}\psi\\&+P_{g11}^{(c2)}\frac{\partial^2\varphi}{\partial x^2}+P_{g22}^{(c2)}\frac{\partial^2\varphi}{\partial y^2}+P_{\mu11}^{(c2)}\frac{\partial^2\psi}{\partial x^2}+P_{\mu22}^{(c2)}\frac{\partial^2\psi}{\partial y^2}-P_{g33}^{(s)}-P_{\mu33}^{(s)}=0.\end{aligned}\tag{54g}$$

2.9 Solution procedure

The Navier approach is applied to obtain the response of the MEE nanoplate under simple supported boundary conditions. A double trigonometric series is used for expanding the seven unknowns as follows (Żur et al. 2020):

$$\begin{pmatrix}u_0\\v_0\\w_b\\w_s\\\phi\\\varphi\\\psi\end{pmatrix}=\sum_{m=1}^{\infty}\sum_{n=1}^{\infty}\begin{pmatrix}\overline{u}cos\left(\alpha x\right)sin\left(\beta y\right)e^{i\omega t}\\\overline{v}sin\left(\alpha x\right)cos\left(\beta y\right)e^{i\omega t}\\\overline{w}_b sin\left(\alpha x\right)sin\left(\beta y\right)e^{i\omega t}\\\overline{w}_s sin\left(\alpha x\right)sin\left(\beta y\right)e^{i\omega t}\\\overline{\phi}sin\left(\alpha x\right)sin\left(\beta y\right)e^{i\omega t}\\\overline{\varphi}sin\left(\alpha x\right)sin\left(\beta y\right)e^{i\omega t}\\\psi sin\left(\alpha x\right)sin\left(\beta y\right)e^{i\omega t}\end{pmatrix},\qquad\alpha=\frac{m\pi}{a},\beta=\frac{n\pi}{b},\tag{55}$$

where $\overline{u}$, $\overline{v}$, $\overline{w}_b$, $\overline{w}_s$, $\overline{\phi}$, $\overline{\varphi}$, and $\overline{\psi}$ define the maximum displacement, the electric potential, and the magnetic potential, respectively. Additionally, w is the natural frequency. The variables can be written as follows:

$$\{\Delta\}=\left[\overline{u}\quad\overline{v}\quad\overline{w}_b\quad\overline{w}_s\quad\overline{\phi}\quad\overline{\varphi}\quad\overline{\psi}\right]^T.\tag{56}$$

The governing equations for the sandwich structure are derived as given below:

$$\left\{[K]-\omega_{mn}^2[M]\right\}\{\Delta\}=\{F\},\tag{57}$$

where $[K]$, $[M]$, and $\{F\}$ define the stiffness, the mass matrix, and the force vector, respectively. Here, the force vector can be written as (Żur et al. 2020)

$$\{F\}=\left[0\quad0\quad0\quad0\quad-\left(B_{e33}^{(g)}+B_{q33}^{(g)}\right)\quad-\left(P_{g33}^{(g)}+P_{e33}^{(g)}\right)\quad-\left(P_{g33}^{(g)}+P_{e33}^{(g)}\right)\right]^T.\tag{58}$$

For free vibration, Eq. (57) may be rearranged as shown below:

$$\left\{[K]-\omega_{mn}^{2}[M]\right\}\{\Delta\}=\{0\}. \tag{59}$$

A mathematical description of the MEE coefficients is given in Appendices (A1)–(A3). The elements of the stiffness and mass matrices are presented in Appendices (A4)–(A5).

Additionally, for buckling analysis, Eq. (57) can be modified as follows:

$$[K]\{\Delta\}=\{0\}. \tag{60}$$

3 Numerical results and discussion

In this section, first, a validation study is performed for the proposed method. Then, the proven approach is applied to analyze the temperature-dependent effective material coefficients and free vibration response of the MEE nanoplate under electric, magnetic, and thermal loads. The structural dimensions of the auxetic core structure and MEE plate layers used in the numerical analysis are given by $a=b=1$, $h=a/25$, $h_{\mathrm{s}}=0.4h$, $h_{\mathrm{r}}=0.1h$,and $h_{\mathrm{p}}=0.2h$.

3.1 Model verification

To assess the reliability of the current method, a comparison is made with two examples of published scientific research. The initial investigation compares the first five natural frequencies of a composite plate, which are simulated using the CUF method under thermal loads, with the results obtained in the present study (Azzara et al. 2023a). The dimensions of the plate are $a=1$ m, $h=0.01$ m, and $a/h=100$. The material properties of the plate structure are: $E_1=144.8$ GPa, $E_2=E_3=9.65$ GPa, $v_{12}=0.3$, $G_{12}=G_{13}=4.14$ GPa, $G_{23}=3.45$ GPa, $\rho=1450$ kg/m^3, $\alpha_{11}=-2.6279\times10^{-7\mathrm{o}}\mathrm{C}^{-1}$, and $\alpha_{12}=30.535\times10^{-6\mathrm{o}}\mathrm{C}^{-1}$. Table 4 shows the assessment of the dimensionless frequency values gained from the present study with the findings obtained from (Azzara et al. 2023b). In accordance with the data presented in this table, the results obtained from the CUF model and the current model are completely compatible with one another.

In the second verification work, the nondimensional frequency values of the rectangular and square plates for various a/b and a/h ratios and nonlocal parameter ea are examined under simply supported boundary conditions and compared with the results obtained by Aghababaei and Reddy (2009). In the analyses, the material properties and dimensions of the plates were set to $a=10$, $v=0.3$, and $E=300\times10^6$ Pa. The following equation is

Table 4 Comparison of the first five natural frequencies for CUF and SHSDT

Mode	Ref. (Azzara et al. 2023b)	Present Study
(1,1)	108.67	107.94
(2,1)	144.30	142.96
(3,1)	222.98	220.03
(1,2)	283.06	279.45
(2,2)	304.53	301.26

Table 5 Comparison of the dimensionless natural frequencies $\overline{\omega}_{11}$, $\overline{\omega}_{22}$, and $\overline{\omega}_{33}$ of the plate structure

Frequencies	ea	Classical	FSDT (Aghababaei and Reddy 2009)	TSDT (Aghababaei and Reddy 2009)	Present (SHSDT)
	0	0.0963	0.0930	0.0935	0.0932
	1	0.0880	0.0850	0.0854	0.0851
ω_{11}	2	0.0816	0.0788	0.0791	0.0785
	3	0.0763	0.0737	0.0741	0.0739
	4	0.0720	0.0696	0.0699	0.0699
	0	0.3853	0.3414	0.3458	0.3410
	1	0.2880	0.2552	0.2585	0.2555
ω_{22}	2	0.2399	0.2126	0.2153	0.2129
	3	0.2099	0.1860	0.1884	0.1862
	4	0.1889	0.1674	0.1696	0.1677
	0	0.8669	0.6889	0.7020	0.6890
	1	0.5202	0.4134	0.4213	0.4132
ω_{33}	2	0.4063	0.3228	0.3290	0.3230
	3	0.3446	0.2738	0.2790	0.2735
	4	0.3045	0.2420	0.2466	0.2422

used to compare the natural frequencies:

$$\overline{\omega} = \omega h \sqrt{\frac{\rho}{G}}. \tag{61}$$

Table 5 depicts the variations in the first three nondimensional frequencies $\overline{\omega}_{11}$, $\overline{\omega}_{22}$, and $\overline{\omega}_{33}$ of the plate according to the three different plate theories and the proposed method. According to this table, there is a high degree of agreement between the numerical results derived from the present investigation and those from the reference study.

3.2 Effective material properties of the auxetic core

In this section, the effects of the geometrical parameters β_3 and θ of the auxetic core cell on the effective material properties, such as the modulus of elasticity E, shear modulus G, Poisson's ratio v, density ρ, and thermal expansion coefficient α, are investigated through Figs. 2–5 for $\Delta T = 0$, the material size parameter $l_m = 0$, the nonlocal parameter $e_0 a = 0$, $\beta_1 = 1.5$ and $\beta_3 = 0.1,\ 0.15,\ 0.20$ and 0.25.

In Fig. 2, the variation in the effective modulus of elasticity and density in the xx and yy directions according to β_3 and the cell inclination angle θ is discussed. An examination of Fig. 2a shows that the modulus of elasticity increases nonlinearly with increasing θ. A slight increase in E_{11} is observed by increasing θ to approximately 70°. However, this increase is quite high at θ values greater than 70°, especially for high values of β_3. For $\beta_3 = 0.25$, the modulus of elasticity in the xx plane (E_{11}) is obtained as 0.02963×10^{11} Pa for $\theta = 45°$, while this value is obtained as 0.1017×10^{11} Pa for $\theta = 70°$ and 3.0240×10^{11} Pa for $\theta = 89°$. When Fig. 2b is examined, it is determined that the modulus of elasticity in the yy direction (E_{22}) increases with increasing β_3 and decreases with increasing θ. While E_{22} decreases rapidly between $\theta = 0°$ and $\theta = 30°$, it decreases more slowly between $\theta = 30°$

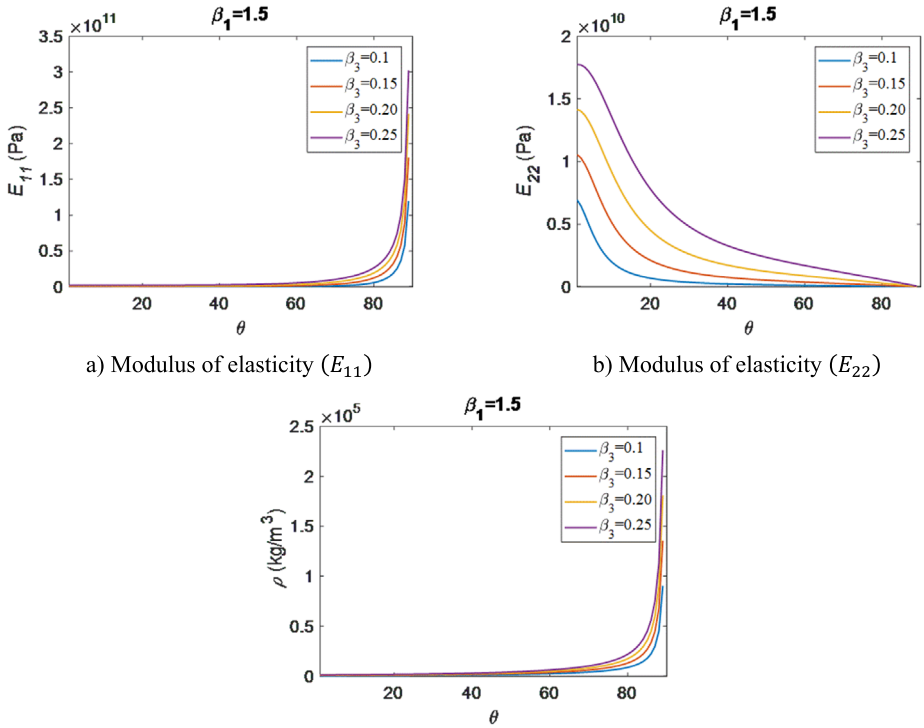

a) Modulus of elasticity (E_{11})

b) Modulus of elasticity (E_{22})

c) Density

Fig. 2 Evaluation of the effective modulus of elasticity and density of the auxetic core layer depending on the inclined angle θ for $\beta_3 = 0.1, 0.15, 0.20$, and 0.25

and $\theta = 90°$. For $\beta_3 = 0.25$, E_{22} is obtained as 0.11×10^{11} Pa for $\theta = 15°$, while this value is obtained as 0.009098×10^{11} Pa for $\theta = 75°$. In Fig. 2c, it is determined that the auxetic core density ρ increases nonlinearly with both β_3 and θ. This increase is quite high, especially for high values of β_3.

Figure 3 displays the variation in the shear modulus values of the auxetic core in the xy, xz, and yz planes according to β_3 and θ. An examination of Fig. 3a and Fig. 3b reveals that for a constant $\beta_1 = 1.5$, G_{12} and G_{13} increase nonlinearly with increasing θ and β_3. In both figures, high shear modulus values are obtained for high values of β_3. In Fig. 3c, the highest shear modulus values are similarly obtained for $\beta_3 = 0.25$. When the shear modulus increases between $\theta = 0°$ and $\theta = 43°$, a decrease is observed after approximately $\theta = 43°$.

Figure 4 provides an evaluation of the change in Poisson's ratio in the xy and yx planes according to β_3 and θ. Here, a negative Poisson's ratio can be observed for the auxetic core layer. Figure 4a demonstrates that higher values of Poisson's ratios are obtained as β_3 decreases. Additionally, this figure shows that higher f Poisson's ratios are obtained as θ increases. Increasing θ up to approximately 50^0 causes Poisson's ratio to increase slightly, regardless of the β_3 value. However, this increasing trend becomes more pronounced, especially after $\theta = 60°$. Similarly, in Fig. 4b, a rise in β_3 leads to a drop in Poisson's ratio. In Fig. 4a, as θ approaches 90°, Poisson's ratio v_{12} exhibits an increasing trend. Conversely, in Fig. 4b, as θ approaches 90°, Poisson's ratio v_{21} demonstrates a decreasing pattern.

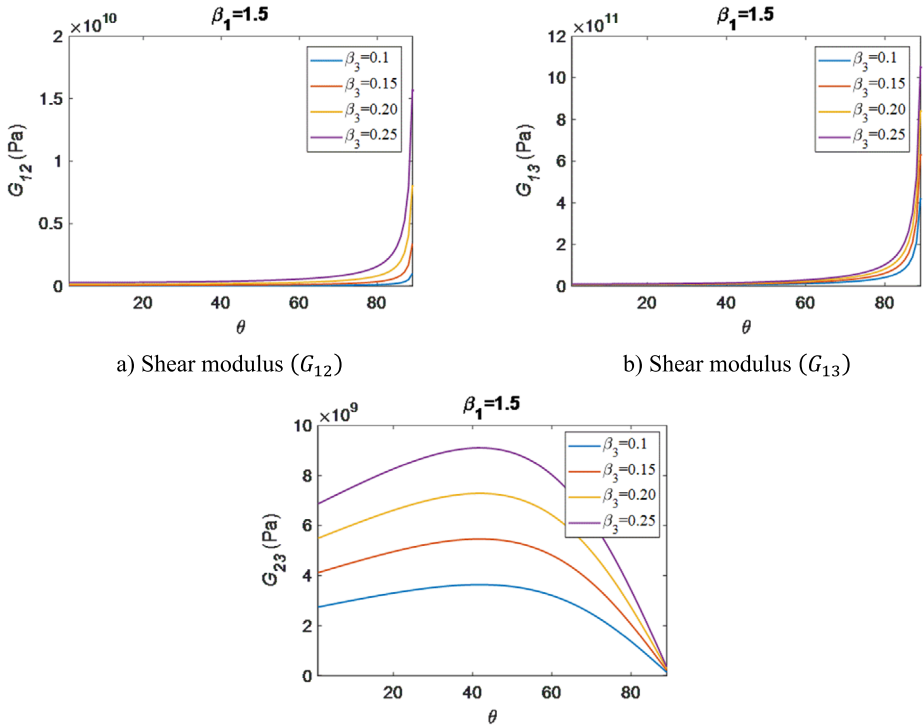

a) Shear modulus (G_{12})

b) Shear modulus (G_{13})

c) Shear modulus (G_{23})

Fig. 3 Evaluation of the effective shear modulus of the auxetic core layer versus the inclined angle θ for $\beta_3 = 0.1, 0.15, 0.20$, and 0.25

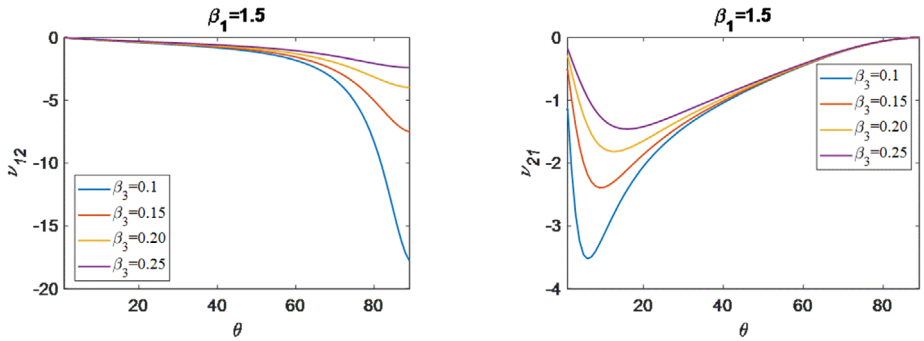

a) Poisson ratio (v_{12})

b) Poisson ratio (v_{21})

Fig. 4 Evaluation of effective Poisson's ratio of the auxetic core layer depending on the inclined angle θ for $\beta_3 = 0.1, 0.15, 0.20$, and 0.25

Figure 5 assesses the variation in the thermal expansion coefficient according to β_3 and θ in the xx and yy planes. The figures illustrate that as θ grows, α_{11} exhibits a linear drop, while α_{22} demonstrates a nonlinear increase. As β_3 increases, both α_{11} and α_{22} also increase.

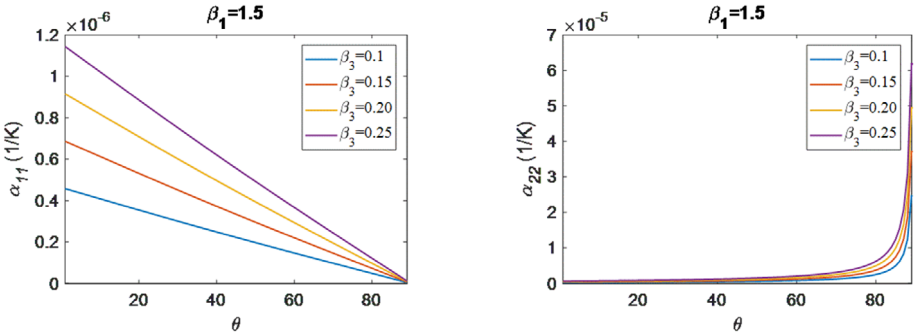

a) Thermal expansion coefficient (α_{11}) b) Thermal expansion coefficient (α_{22})

Fig. 5 Evaluation of the effective thermal expansion coefficient of the auxetic core layer versus the inclined angle θ for $\beta_3 = 0.1, 0.15, 0.20$, and 0.25

3.3 Free vibration analysis of the FGM sandwich nanoplate

In this subsection, the frequency response analysis of the sandwich nanoplate with an auxetic core is examined with respect to the parameters of temperature rise, electrical load, magnetic load, nonlocal parameter, and material size factor. The input magnetic field is defined by Eq. (62), and the electric field is defined by Eq. (63).

$$H_m = \frac{H_0}{D}, \quad D = \frac{EH^3}{12\left(1-\nu^2\right)}. \tag{62}$$

$$V_m = \frac{V_0}{D}, \quad D = \frac{EH^3}{12\left(1-\nu^2\right)}. \tag{63}$$

Figure 6 exhibits the effects of the temperature difference ΔT, cell inclination angle θ, and β_3 on the nondimensional frequency λ_1 of the sandwich nanoplate. As shown in Fig. 6a-b, the first dimensionless frequency of the sandwich nanoplate decreases as both β_3 and ΔT increase. The reason for this decrease in the dimensionless frequency is the decrease in the modulus of elasticity of all the materials in the sandwich plate with increasing temperature and, accordingly, the drop in the stiffness of the structure. Another reason for the decrease in the dimensionless frequency is that the stiffness of the auxetic core increases as β_3 increases, but the mass increases more than the stiffness. For β_3 values of 0.10, 0.15, 0.20, and 0.25, the buckling temperature of the sandwich plate is calculated as 267 K, 264 K, 258.50 K, and 250.50 K for Fig. 6a, 262.40 K, 256 K, 246 K, and 236 K for Fig. 6b, and 249 K, 231 K, 226 K, and 254.50 K for Fig. 6c, respectively. As can be seen, the buckling temperature decreases with increasing β_3. An examination of Fig. 6d reveals that the natural frequency and buckling temperature decrease with increasing θ.

Figure 7 evaluates the influence of ΔT, θ, and β_1 on the nondimensional frequency of the MEE sandwich nanoplate. As shown in Figure, the first dimensionless frequency and buckling temperature of the sandwich nanoplate increase as β_1 increases. For β_1 values of 1, 1.5, 2, and 2.5, the buckling temperature of the sandwich plate is calculated as 253.5 K, 265 K, 267 K, and 269 K for Fig. 7a, 195.5 K, 256 K, 265.5 K, and 267.5 K for Fig. 7b, and 188 K, 231.5 K, 259.5 K, and 265 K for Fig. 7c, respectively. When Fig. 7d is examined, it is concluded that the natural frequency and buckling temperature decrease with increasing θ.

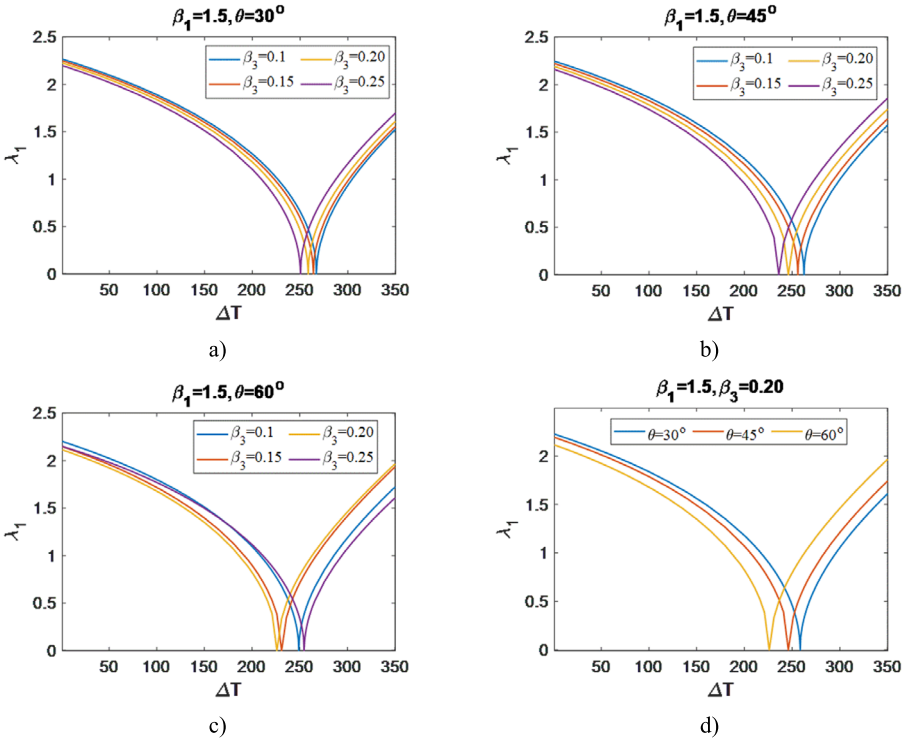

Fig. 6 Variation in the dimensionless frequency λ_1 depending on the β_3 and θ values of the auxetic core and temperature rise ΔT; applied electric load $V_m = 0$; and applied magnetic load $H_m = 0$

The variation in the dimensionless frequency of the sandwich nanoplate with respect to the thermal and electrical load is shown in Fig. 8 for three different $BaTiO_3$ and $CoFe_2O_4$ mixing ratios. In the analysis, four different voltage values are applied ($V_m = 0$, 0.1, 0.2, and 0.3). Figure 8a exhibits the effect of the four different voltage parameters upon the first nondimensional natural frequency. As shown in Fig. 8a-c, the dimensionless first frequency values decline as the temperature difference increases. It is also seen from the figure that increasing voltage has a decreasing effect on the natural frequency and buckling temperature. For example, in Fig. 8a, when no voltage is applied, the dimensionless natural frequency is obtained as 1.25 for ΔT =150, while this value is 1.24 for $V_m = 0.1$, 1.02 for $V_m = 0.2$, and 0.88 for $V_m = 0.3$. In addition, the buckling temperatures for $V_m = 0$, 0.1, 0.2, and 0.3 are obtained as 222 K, 210 K, 199 K, and 187 K, respectively. In Fig. 8b, the material composition ratio of the MEE plate is $BaTiO_3 = 0.3$ and $CoFeO_4 = 0.7$. As can be seen, the natural frequency and buckling temperatures increased with increasing $CoFeO_4$ ratio. When the $V_m = 0$ curves in Fig. 8a-b are examined, it is understood that the increase in the natural frequency is attributed to the higher stiffness property of $CoFe_2O_4$ compared to $BaTiO_3$. Again, when Fig. 8b is examined, the natural frequency decreases with increasing electrical load. However, according to Fig. 8a, with decreasing $BaTiO_3$ concentration, the rate of drop in the natural frequency decreased. This is due to the piezoelectric behavior of $BaTiO_3$. When no voltage is applied for the $BaTiO_3 = 0.3$ and $CoFe_2O_4 = 0.7$ ratios, the dimensionless natural frequency is 1.28 for a ΔT =150, while this value is 1.23 for $V_m = 0.1$, 1.16 for $V_m = 0.2$, and 1.10 for $V_m = 0.3$. In addition, the buckling tempera-

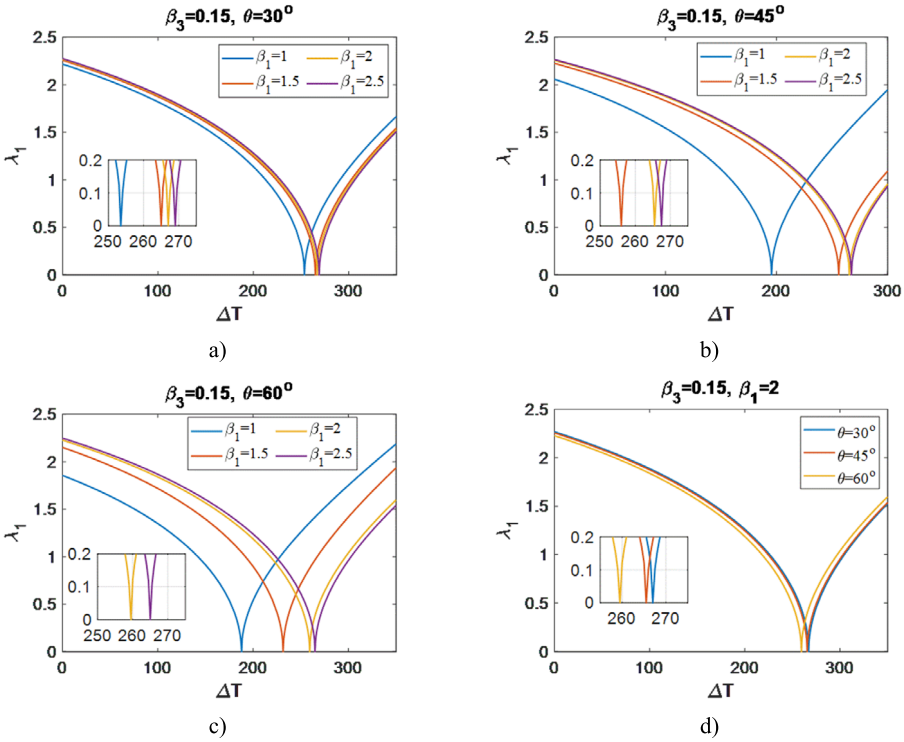

Fig. 7 Variation of the dimensionless frequencies λ_1 depending on the β_1 and θ values of the auxetic core and temperature rise ΔT; applied electric load $V_m = 0$; applied magnetic load $H_m = 0$

tures for $V_m = 0$, $V_m = 0.1$, $V_m = 0.2$, and $V_m = 0.3$ are obtained as 229 K, 223 K, 216 K, and 210 K, respectively. The variation in the nondimensional fundamental frequency of the sandwich nanoplate with respect to temperature and electrical charge for $BaTiO_3 = 0.7$ and $CoFe_2O_4 = 0.3$ is shown in Fig. 8c. As shown in the figure, with increasing $BaTiO_3$ ratio in the MEE plate, the dimensionless natural frequency decreased due to the stiffness of $BaTiO_3$ and $CoFe_2O_4$. In addition, the piezoelectric property of the MEE plate increased with increasing $BaTiO_3$ ratio, thus a significant decrease in the natural frequency and buckling temperature occurred.

The fluctuations in the dimensionless frequency of the sandwich nanoplate with respect to thermal and magnetic loads are shown in Fig. 9 for three different $BaTiO_3$ and $CoFe_2O_4$ mixing ratios. In the analysis, four different magnetic field loads are applied ($H_m = 0, 0.001, 0.002, 0.003$). Figure 9a shows the effect of four different magnetic load parameters on the first dimensionless natural frequency for $BaTiO_3 = 0.5$ and $CoFe_2O_4 = 0.5$. As depicted in the figure, increasing temperature has a decreasing effect on the dimensionless natural frequency, while increasing magnetic field load has an increasing effect on the natural frequency. In addition, increasing magnetic field load also increases the buckling temperature of the plate. For example, in Fig. 9a, for $H_m = 0$, the dimensionless natural frequency is 1.62 for ΔT =150, while this value is 1.50 for $H_m = 0.001$, 1.38 for $H_m = 0.002$, and 1.25 for $H_m = 0.003$. In addition, the buckling temperatures for $H_m = 0, 0.001, 0.002$, and 0.003 are 222 K, 236 K, 249 K, and 263 K, respectively. The effect of the magnetic field load on the dimensionless natural frequency of the sandwich plate for $BaTiO_3 = 0.3$ and $CoFe_2O_4 = 0.7$

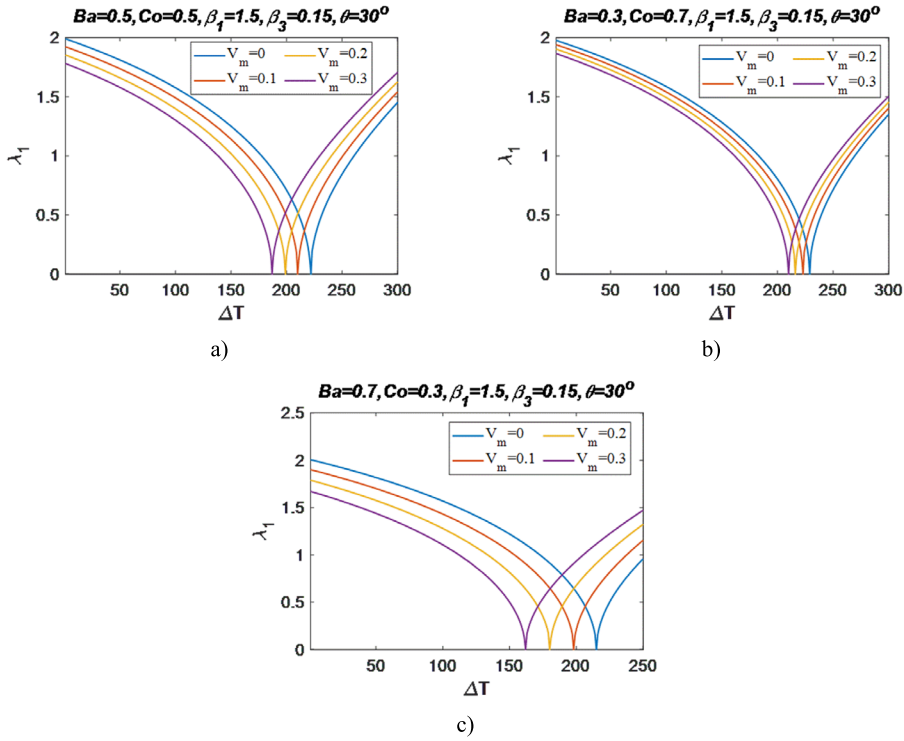

Fig. 8 Variation in the dimensionless frequency λ_1 depending on the temperature rise and electrical load; for the face plate material mixture $BaTiO_3$ 70%, 50%, and 30% and $CoFe_2O_3$ %30, 50%, and 70%; applied magnetic load $H_m = 0$

is investigated with Fig. 9b. As illustrated in the figure, the natural frequency and buckling temperature increase with the increasing $CoFe_2O_4$ ratio in the MEE face plate. Increasing $CoFe_2O_4$ ratio has two effects on the natural frequency and buckling. First, the natural frequency and buckling temperature of the plate directly increase due to the high stiffness of $CoFe_2O_4$. Second, the magnetic behavior of the MEE face plates increases with increasing $CoFe_2O_4$ concentration, which increases the natural frequency of the plate and the buckling temperature. The effects of $BaTiO_3 = 0.7$ and $CoFe_2O_4 = 0.3$ on the natural frequency and buckling temperature are depicted in Fig. 9c. With the dominance of the $BaTiO_3$ ratio in the MEE face plate, the natural frequency of the plate decreased due to the low Young's modulus of $BaTiO_3$ compared to that of $CoFe_2O_4$. However, the natural frequency increased with the effect of the applied magnetic field. It can be concluded from Fig. 9 that the magnetic field has a stiffness increasing effect on the plate.

Figure 10a presents the variation in the nondimensional natural frequency and buckling temperature of the nanoplate depending on the nonlocal parameters e_0a and ΔT. An evaluation of the figure demonstrates that the natural frequency decreases with increasing e_0a and ΔT. When the buckling temperature is 265 K for $e_0a = 0$, it drops to 58 K for $e_0a = 0.5$ nm^2. In Fig. 10b, the variation in the natural frequency of the sandwich nanoplate with respect to the temperature difference is shown for material size factors $l_m = 0$, 1, 1.41, and 2 nm^2. As shown in the figure, the dimensionless natural frequency of the plate increases as the material size factor increases. When the buckling temperature is 265 K for $l_m = 0$, it

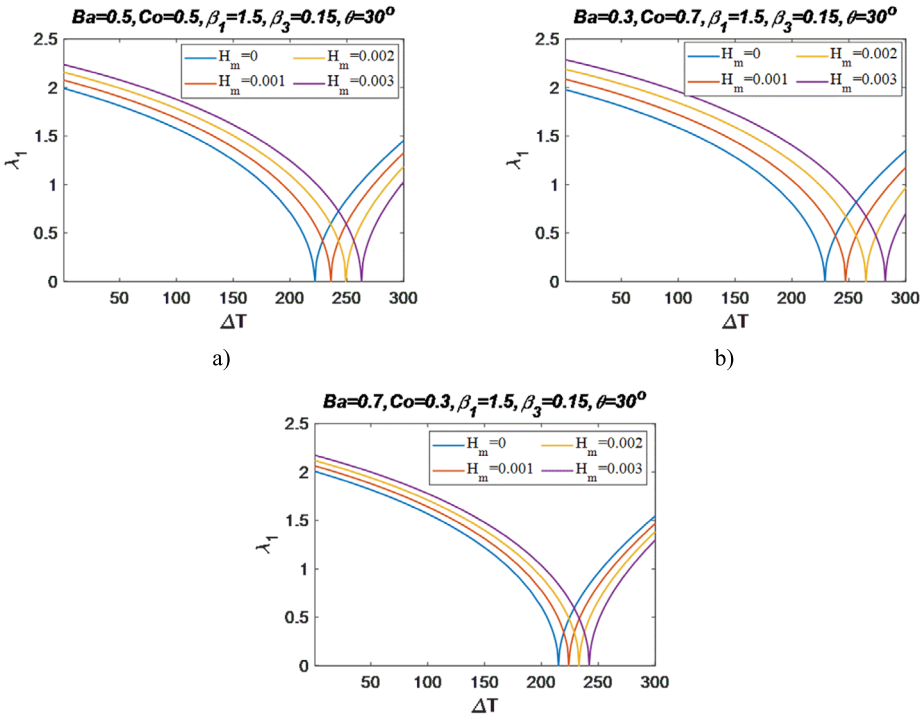

Fig. 9 Variation in the dimensionless frequency λ_1 depending on the temperature rise and magnetic load; for the face plate material mixture $BaTiO_3$ 70%, 50%, and 30% and $CoFe_2O_3$ %30, 50%, and 70%; applied electric load $V_m = 0$

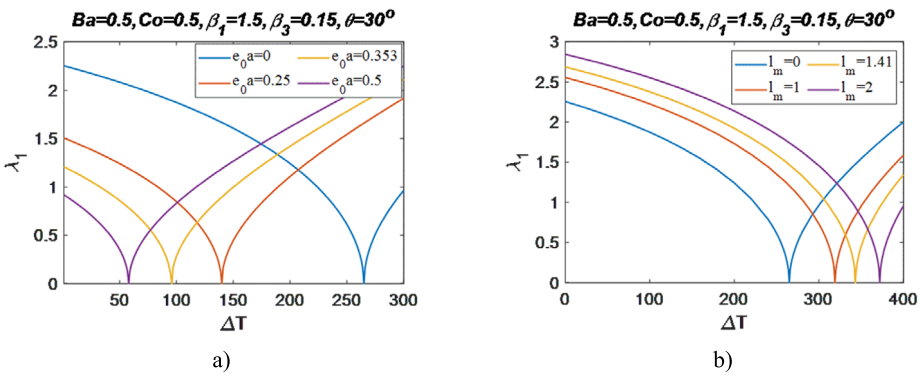

Fig. 10 Variation in the dimensionless frequency λ_1 depending on the nonlocal parameter e_0a and material size parameter l_m; applied electric load $V_m = 0$; applied magnetic load $H_m = 0$

increases to 372 K for $l_m = 2$ nm^2. A general evaluation of Fig. 10 shows that while the nonlocal parameter and temperature difference have similar effects on decreasing the natural frequency, the material size factor has an effect on increasing the natural frequency.

4 Conclusions

In this study, the thermomechanical free vibration and buckling behavior of smart sandwich nanostructures with auxetic cores and MEE face layers were investigated using SHSDT and NSGT. While the material properties of the face plates are determined by the rule of mixture, the material properties of the auxetic core layer vary according to the β_1, β_3, and θ parameters. First, the influence of various β_3 and θ parameters with respect to nonlinear temperature fluctuations was examined to determine the effective material properties (modulus of elasticity, shear modulus, Poisson's ratio, thermal expansion, and density). As a consequence, the findings that have been gained from performing these computational models are expressed as follows:

The elastic modulus of the auxetic core layer in the xx direction (E_{11}) exhibits a nonlinear increase with increasing θ and β_3. On the other hand, the modulus of elasticity in the yy direction (E_{22}) exhibits an increase with increasing β_3 and a reduction with rising θ. Therefore, the elastic modulus of the auxetic core layer in the x and y directions can be adjusted using the θ, thickness and aspect ratio parameters of the auxetic core. This feature offers the possibility to adjust the elastic modulus in the sandwich nanoplate depending on the directions.

Higher values of v_{12} are obtained as β_3 decreases. Additionally, higher values of v_{12} are obtained as θ increases. A rise in β_3 leads to a decrease in v_{21}. Depending on θ, v_{12} increases negatively close to linear between $\theta = 1°$ and $\theta = 50°$. In the range of $\theta = 50°$ and $\theta = 89°$, it shows a nonlinear parabolic trend. For $\beta_1 = 1.5$ and $\theta = 80°$, v_{12} increases negatively to -2.1178 at $\beta_3 = 0.25$ and -9.2511 at $\beta_3 = 0.1$. For $\beta_1 = 1.5$ and $\theta = 6°$, v_{21} increases negatively to -0.9548 at $\beta_3 = 0.25$ and -3.5233 at $\beta_3 = 0.1$. Therefore, the negative Poisson's ratios can be tuned in the xy and yx directions and thus the metamaterial properties can be adjusted.

When weight control and lightweight design are required, the mass density ρ of the auxetic core can be adjusted with the auxetic core parameters. The auxetic core layer density increases nonlinearly with both β_3 and θ. This increase is quite high, especially for high values of β_3.

The variation of the shear modulus also varies significantly in auxetic core in a nonlinear manner depending on the parameters. The shear modulus values G_{12} and G_{13} increase nonlinearly with increasing θ and β_3. High shear modulus values are obtained for high values of β_3.

The coefficient of thermal expansion of the auxetic core can also be tuned. When θ increases, α_{11} exhibits a linear drop, while α_{22} demonstrates a nonlinear increase. As β_3 increases, both α_{11} and α_{22} also increase.

Second, the frequency response and buckling analysis of the sandwich nanoplate were examined with respect to the parameters of temperature rise, electrical load, magnetic load, nonlocal parameter, and material size factor. As a consequence, the findings that have been gained from performing these computational models are expressed as follows:

Besides the thermal effect, the properties of the auxetic core also affect the thermomechanical vibration behaviour of the smart nanoplate. When inclination angle θ and length ratio β_1 of the auxetic core are kept constant, the dimensionless frequency of the MEE nanoplate decreases as both ΔT and β_3 increase.

The increase in the natural frequency and buckling temperature is physically a result of the stiffness and therefore the modulus of elasticity in the smart sandwich nanoplate. In addition, a low coefficient of thermal expansion results in a high buckling temperature and natural frequency. When β_1 and θ are constant, a decrease in the buckling temperature of

the MEE nanoplate is observed as the values of β_3 and θ increase. When β_3 is constant, with the increase in β_1, the MEE nanoplate experiences an increase in both the dimensionless frequency and buckling temperature. Increasing θ causes a decrease in both the dimensionless frequency and the buckling temperature.

Due to the electro-elastic property of the face layers, increasing the electrical load has a decreasing effect on the nondimensional natural frequency and buckling temperature of the sandwich plate. In other words, the electric charge reduces the stiffness of the structure. This property becomes more effective with the increase of $BaTiO_3$ ratio in the surface layers.

Because of the magnetostrictive property of $CoFe_2O_4$ in the face layers, increasing magnetic field load has an increasing impact on the nondimensional natural frequency. Additionally, increasing the magnetic field load increases the buckling temperature of the sandwich plate.

The effect of the size factor creates a strength enhancement effect in the smart nanoplate with the strain gradient elasticity effect. Thus, the dimensionless first natural frequency of the sandwich plate increases as the material size factor increases.

On the contrary, due to the effect of nonlocal integral elasticity, softening effect occurs in the smart nanoplate depending on the nonlocal parameter and, therefore, the nonlocal parameter has a decreasing effect on the natural frequency. In other words, while the material size factor stiffens the plate, the nonlocal parameter softens the plate.

With this study, important inferences were obtained about the thermal buckling and free vibration behavior of sandwich MEE plates with auxetic cores. It is considered that a reference will be provided to the gap in the literature with the analyzes made by considering the temperature-dependent material properties of $BaTiO_3$ and $CoFe_2O_4$.

Appendix

$$
\begin{aligned}
A_{ij}^{(n)} &= \int_{-h/2-h_s}^{-h/2} C_{ij}^{s}\left\{1, z, z^2\right\} dz + \int_{-h/2}^{h/2} C_{ij}^{c}\left\{1, z, z^2\right\} dz \\
&\quad + \int_{h/2}^{h/2+h_s} C_{ij}^{s}\left\{1, z, z^2\right\} dz \quad n = 0, 1, 2 \\
\overline{A}_{ij}^{(\overline{n})} &= \int_{-h/2-h_s}^{-h/2} C_{ij}^{s} f(z)\{1, z, f(z)\} dz + \int_{-h/2}^{h/2} C_{ij}^{c} f(z)\{1, z, f(z)\} dz \\
&\quad + \int_{h/2}^{h/2+h_s} C_{ij}^{s} f(z)\{1, z, f(z)\} dz, \quad \overline{n} = 0, 1, f \\
\tilde{A}_{ij}^{(\tilde{n})} &= \int_{-h/2-h_s}^{-h/2} C_{ij}^{s} g^{'}(z)\left\{1, z, g'(z), f(z)\right\} dz \\
&\quad + \int_{-h/2}^{h/2} C_{ij}^{c} g^{'}(z)\left\{1, z, g'(z), f(z)\right\} dz \\
&\quad + \int_{h/2}^{h/2+h_s} C_{ij}^{s} g'(z)\{1, z, g^{'}(z), f(z)\} dz, \overline{n} = 0, 1, g^{'}, f \\
\tilde{A}_{ij}^{(\tilde{n})} &= \int_{-h/2-h_s}^{-h/2} C_{ij}^{s} g^2(z) dz + \int_{-h/2}^{h/2} C_{ij}^{c} g^2(z) dz + \int_{h/2}^{h/2+h_s} C_{ij}^{s} g^2(z) dz
\end{aligned}
\tag{A1}
$$

$$
\begin{aligned}
B_{e_{ij}}^{(k)} = -\Bigg[& \int_{-h/2-h_s}^{-h/2} e_{ij}\left(\frac{2\varphi_0}{h_s}\right)\left\{z, f(z), g'(z), \left(\frac{h_s}{2\varphi_0}\right) cos\left(\frac{\pi z_2}{h_s}\right)\right\} dz \\
& + \int_{-h/2}^{h/2} e_{ij}\left(\frac{2\varphi_0}{h}\right)\left\{z, f(z), g'(z), \left(\frac{h_s}{2\varphi_0}\right) cos\left(\frac{\pi z}{h_s}\right)\right\} dz \\
& + \int_{h/2}^{h/2+h_s} e_{ij}\left(\frac{2\varphi_0}{h_s}\right)\left\{z, f(z), g'(z), \left(\frac{h_s}{2\varphi_0}\right) cos\left(\frac{\pi z_2}{h_s}\right)\right\} dz\Bigg], \quad k = 1, f, g', g \\
\overline{B}_{e_{ij}}^{(k)} = -\Bigg[& \int_{-h/2-h_s}^{-h/2} e_{ij}\left[\frac{\pi}{h_s} sin\left(\frac{\pi z_1}{h_s}\right)\right]\left\{1, z, f(z), g'(z)\right\} dz \\
& + \int_{-h/2}^{h/2} e_{ij}\left[\frac{\pi}{h} sin\left(\frac{\pi z}{h}\right)\right]\left\{1, z, f(z), g'(z)\right\} dz \\
& + \int_{h/2}^{h/2+h_s} e_{ij}\left[\frac{\pi}{h_s} sin\left(\frac{\pi z_2}{h_s}\right)\right]\left\{1, z, f(z), g'(z)\right\} dz\Bigg], \quad k = 0, 1, f, g' \\
B_{q_{ij}}^{(k)} = -\Bigg[& \int_{-h/2-h_s}^{-h/2} q_{ij}\left(\frac{2\varphi_0}{h_s}\right)\left\{z, f(z), g'(z), \left(\frac{h_f}{2\varphi_0}\right) cos\left(\frac{\pi z_1}{h_s}\right)\right\} dz \\
& + \int_{-h/2}^{h/2} q_{ij}\left(\frac{2\varphi_0}{h}\right)\left\{z, f(z), g'(z), \left(\frac{h}{2\varphi_0}\right) cos\left(\frac{\pi z}{h}\right)\right\} dz \\
& + \int_{h/2}^{h/2+h_s} q_{ij}\left(\frac{2\varphi_0}{h_s}\right)\left\{z, f(z), g'(z), \left(\frac{h_f}{2\varphi_0}\right) cos\left(\frac{\pi z_2}{h_s}\right)\right\} dz\Bigg], \quad k = 1, f, g', g \\
\overline{B}_{q_{ij}}^{(k)} = -\Bigg[& \int_{-h/2-h_s}^{-h/2} q_{ij}\left[\frac{\pi}{h_s} sin\left(\frac{\pi z_1}{h_s}\right)\right]\left\{1, z, f(z), g'(z)\right\} dz \\
& + \int_{-h/2}^{h/2} q_{ij}\left[\frac{\pi}{h} sin\left(\frac{\pi z}{h}\right)\right]\left\{1, z, f(z), g'(z)\right\} dz \\
& + \int_{h/2}^{h/2+h_s} q_{ij}\left[\frac{\pi}{h_s} sin\left(\frac{\pi z_2}{h_s}\right)\right]\left\{1, z, f(z), g'(z)\right\} dz\Bigg], \quad k = 0, 1, f, g' \\
P_{\varepsilon_{ij}}^{(n)} = -\Bigg[& \int_{-h/2-h_s}^{-h/2} \varepsilon_{ij}\left\{\left(\frac{2\varphi_0}{h_s}\right)\left[\frac{\pi}{h_s} sin\left(\frac{\pi z_1}{h_s}\right)\right], \right. \\
& \left. \left[\frac{\pi}{h_s} sin\left(\frac{\pi z_1}{h_s}\right)\right]^2, \left[cos\left(\frac{\pi z_1}{h_s}\right)\right]^2\right\} dz \\
& + \int_{-h/2}^{h/2} \varepsilon_{ij}\left\{\left(\frac{2\varphi_0}{h}\right)\left[\frac{\pi}{h} sin\left(\frac{\pi z}{h}\right)\right], \left[\frac{\pi}{h} sin\left(\frac{\pi z}{h}\right)\right]^2, \left[cos\left(\frac{\pi z}{h}\right)\right]^2\right\} dz \\
& + \int_{h/2}^{h/2+h_s} \varepsilon_{ij}\left\{\left(\frac{2\varphi_0}{h_s}\right)\left[\frac{\pi}{h_s} sin\left(\frac{\pi z_2}{h_s}\right)\right], \right. \\
& \left. \left[\frac{\pi}{h_s} sin\left(\frac{\pi z_2}{h_s}\right)\right]^2, \left[cos\left(\frac{\pi z_2}{h_s}\right)\right]^2\right\} dz\Bigg], \\
& n = 1, s2, c2
\end{aligned}
\tag{A2}
$$

$$
\begin{aligned}
P_{g_{ij}}^{(n)} = -\Bigg[& \int_{-h/2-h_s}^{-h/2} g_{ij} \left\{ \left(\frac{2\varphi_0}{h_s}\right) \left[\frac{\pi}{h_s} sin\left(\frac{\pi z_1}{h_s}\right)\right], \right. \\
& \left. \left[\frac{\pi}{h_s} sin\left(\frac{\pi z_1}{h_s}\right)\right]^2, \left[cos\left(\frac{\pi z_1}{h_s}\right)\right]^2 \right\} dz \\
& + \int_{-h/2}^{h/2} g_{ij} \left\{ \left(\frac{2\varphi_0}{h}\right) \left[\frac{\pi}{h} sin\left(\frac{\pi z}{h}\right)\right], \left[\frac{\pi}{h} sin\left(\frac{\pi z}{h}\right)\right]^2, \left[cos\left(\frac{\pi z}{h}\right)\right]^2 \right\} dz \\
& + \int_{h/2}^{h/2+h} g_{ij} \left\{ \left(\frac{2\varphi_0}{h_s}\right) \left[\frac{\pi}{h_s} sin\left(\frac{\pi z_2}{h_s}\right)\right], \right. \\
& \left. \left[\frac{\pi}{h_s} sin\left(\frac{\pi z_2}{h_s}\right)\right]^2, \left[cos\left(\frac{\pi z_2}{h_s}\right)\right]^2 \right\} dz \Bigg], \\
& n = 1, s2, c2
\end{aligned}
\tag{A3}
$$

$$
\begin{aligned}
P_{\mu_{ij}}^{(n)} = -\Bigg[& \int_{-h/2-h_s}^{-h/2} \mu_{ij} \left\{ \left(\frac{2\varphi_0}{h_s}\right) \left[\frac{\pi}{h_s} sin\left(\frac{\pi z_1}{h_s}\right)\right], \right. \\
& \left. \left[\frac{\pi}{h_s} sin\left(\frac{\pi z_1}{h_s}\right)\right]^2, \left[cos\left(\frac{\pi z_1}{h_s}\right)\right]^2 \right\} dz \\
& + \int_{-h/2}^{h/2} \mu_{ij} \left\{ \left(\frac{2\varphi_0}{h}\right) \left[\frac{\pi}{h} sin\left(\frac{\pi z}{h}\right)\right], \left[\frac{\pi}{h} sin\left(\frac{\pi z}{h}\right)\right]^2, \left[cos\left(\frac{\pi z}{h}\right)\right]^2 \right\} dz \\
& + \int_{h/2}^{h/2+h_s} \mu_{ij} \left\{ \left(\frac{2\varphi_0}{h_s}\right) \left[\frac{\pi}{h_s} sin\left(\frac{\pi z_2}{h_s}\right)\right], \right. \\
& \left. \left[\frac{\pi}{h_s} sin\left(\frac{\pi z_2}{h_s}\right)\right]^2, \left[cos\left(\frac{\pi z_2}{h_s}\right)\right]^2 \right\} dz \Bigg], \\
& n = 1, s2, c2
\end{aligned}
$$

$$K_{11} = -c_2 \left(\alpha^2 A_{11}^{(0)} + \beta^2 A_{66}^{(0)}\right)$$

$$K_{12} = -c_2 \alpha\beta \left(A_{12}^{(0)} + A_{66}^{(0)}\right)$$

$$K_{13} = c_2 \left(\alpha^3 A_{11}^{(1)} + \alpha\beta^2 \left(A_{12}^{(1)} + 2A_{66}^{(1)}\right)\right)$$

$$K_{14} = c_2 \left(\alpha^3 \overline{A}_{11}^{(0)} + \alpha\beta^2 \left(\overline{A}_{12}^{(0)} + 2\overline{A}_{66}^{(0)}\right)\right)$$

$$K_{15} = c_2 \alpha \tilde{A}_{13}^{(0)}$$

$$K_{16} = c_2 \alpha \overline{B}_{e31}^{(0)}$$

$$K_{17} = c_2 \alpha \overline{B}_{q31}^{(0)}$$

$$K_{22} = -c_2 \left(\left(\beta^2 A_{22}^{(0)} + \alpha^2 A_{66}^{(0)}\right)\right)$$

$$K_{23} = -c_2\left(\beta^3 A_{22}^{(1)} + \beta\alpha^2\left(A_{12}^{(1)} + 2A_{66}^{(1)}\right)\right)$$

$$K_{24} = c_2\left(\beta^3 \overline{A}_{22}^{(0)} + \beta\alpha^2\left(\overline{A}_{12}^{(0)} + 2\overline{A}_{66}^{(0)}\right)\right)$$

$$K_{25} = c_2\beta\tilde{A}_{23}^{(0)}$$

$$K_{26} = c_2\beta\overline{B}_{e32}^{(0)}$$

$$K_{27} = c_2\beta\overline{B}_{q32}^{(0)}$$

$$\begin{aligned} K_{33} = {} & \alpha^2\left[1 + \mathcal{B}\left(\alpha^2 + \beta^2\right)\right]\left(N_0 + p_{e31} + p_{q31}\right) \\ & + \beta^2\left[1 + \mathcal{B}\left(\alpha^2 + \beta^2\right)\right]\left(\gamma N_0 + p_{e32} + p_{q32}\right) \\ & - c_2\left(\alpha^4 A_{11}^{(2)} - \beta^4 A_{22}^{(2)} - 2\alpha^2\beta^2\left(A_{12}^{(2)} + 2A_{66}^{(2)}\right)\right) \end{aligned} \tag{A4}$$

$$K_{34} = -c_2\left(\alpha^4 \overline{A}_{11}^{(1)} + \beta^4 \overline{A}_{22}^{(1)} + 2\alpha^2\beta^2\left(\overline{A}_{12}^{(1)} + 2\overline{A}_{66}^{(1)}\right)\right)$$

$$K_{35} = -c_2\left(\alpha^2\tilde{A}_{13}^{(1)} + \beta^2 A_{23}^{(1)}\right)$$

$$K_{36} = -c_2\left(\alpha^2\overline{B}_{e31}^{(1)} + \beta^2\overline{B}_{e32}^{(1)}\right)$$

$$K_{37} = -c_2\left(\alpha^2\overline{B}_{q31}^{(1)} + \beta^2\overline{B}_{q32}^{(1)}\right)$$

$$K_{44} = -c_2\left(\alpha^2\hat{A}_{55}^{(0)} + \beta^2\hat{A}_{44}^{(0)} + \alpha^4\overline{A}_{11}^{(f)} + \beta^4\overline{A}_{22}^{(f)} + 2\alpha^2\beta^2\left(\overline{A}_{12}^{(f)} + 2\overline{A}_{66}^{(f)}\right)\right)$$

$$K_{45} = -c_2\left(\alpha^2\left(\tilde{A}_{13}^{(f)} + \hat{A}_{55}^{(0)}\right) + \beta^2\left(\tilde{A}_{23}^{(f)} + \hat{A}_{44}^{(0)}\right)\right)$$

$$K_{46} = c_2\left(\alpha^2\left(B_{e15}^{(g)} - \overline{B}_{e31}^{(f)}\right) + \beta^2\left(B_{e24}^{(g)} - \overline{B}_{e32}^{(f)}\right)\right)$$

$$K_{47} = c_2\left(\alpha^2\left(B_{q15}^{(g)} - \overline{B}_{q31}^{(f)}\right) + \beta^2\left(B_{q24}^{(g)} - \overline{B}_{q32}^{(f)}\right)\right)$$

$$K_{55} = -c_2\left(\tilde{A}_{33}^{(g)} + \alpha^2\hat{A}_{55}^{(0)} + \beta^2\hat{A}_{44}^{(0)}\right)$$

$$K_{56} = c_2\left(\alpha^2 B_{e15}^{(g)} + \beta^2 B_{e24}^{(g)} - \overline{B}_{e33}^{(g)}\right)$$

$$K_{57} = c_2\left(\alpha^2 B_{q15}^{(g)} + \beta^2 B_{q24}^{(g)} - \overline{B}_{q33}^{(g)}\right)$$

$$K_{66} = c_2\left(\alpha^2 p_{\varepsilon 11}^{(c2)} + \beta^2 p_{\varepsilon 22}^{(c2)} + p_{\varepsilon 33}^{(s2)}\right)$$

$$K_{66} = c_2\left(\alpha^2 p_{g11}^{(c2)} + \beta^2 p_{g22}^{(c2)} + p_{g33}^{(s2)}\right)$$

$$K_{77} = c_2\left(\alpha^2 p_{\mu 11}^{(c2)} + \beta^2 p_{\mu 22}^{(c2)} + p_{\mu 33}^{(s2)}\right)$$

$$c_2 = (1 + l_m(\alpha^2 + \beta^2)$$

$$M_{11} = -\left[1 + \mathcal{B}\left(\alpha^2 + \beta^2\right)\right]m_0$$

$$M_{13} = \alpha\left[1 + \mathcal{B}\left(\alpha^2 + \beta^2\right)\right]m_1$$

$$
\begin{aligned}
M_{14} &= \alpha\left[1+\mathcal{B}\left(\alpha^2+\beta^2\right)\right]m_3 \\
M_{12} &= M_{15} = M_{16} = M_{17} = 0 \\
M_{22} &= -\left[1+\mathcal{B}\left(\alpha^2+\beta^2\right)\right]m_0 \\
M_{23} &= \beta\left[1+\mathcal{B}\left(\alpha^2+\beta^2\right)\right]m_1 \\
M_{24} &= \beta\left[1+\mathcal{B}\left(\alpha^2+\beta^2\right)\right]m_3 \\
M_{25} &= M_{26} = M_{27} = 0 \\
M_{33} &= -\left[1+\mathcal{B}\left(\alpha^2+\beta^2\right)\right]m_0 - \left(\alpha^2+\beta^2\right)\left[1+\mathcal{B}\left(\alpha^2+\beta^2\right)\right]m_2 \\
M_{34} &= -\left[1+\mathcal{B}\left(\alpha^2+\beta^2\right)\right]m_0 - \left(\alpha^2+\beta^2\right)\left[1+\mathcal{B}\left(\alpha^2+\beta^2\right)\right]m_4 \\
M_{35} &= -\left[1+\mathcal{B}\left(\alpha^2+\beta^2\right)\right]m_6 \\
M_{36} &= M_{37} = 0 \\
M_{44} &= -\left[1+\mathcal{B}\left(\alpha^2+\beta^2\right)\right]m_0 - \left(\alpha^2+\beta^2\right)\left[1+\mathcal{B}\left(\alpha^2+\beta^2\right)\right]m_5 \\
M_{45} &= -\left[1+\mathcal{B}\left(\alpha^2+\beta^2\right)\right]m_6 \\
M_{46} &= M_{47} = 0 \\
M_{55} &= -\left[1+\mathcal{B}\left(\alpha^2+\beta^2\right)\right]m_7
\end{aligned}
\tag{A5}
$$

Author contributions Author contributions KGA: conceptualization, methodology, investigation, simulation, writing—original draft, writing—review and editing. FP: investigation, simulation, writing—original draft. IE: supervision, validation, resources, writing—review and editing.

Funding Open access funding provided by the Scientific and Technological Research Council of Türkiye (TÜBİTAK). No funding was received for conducting this study.

Data Availability No datasets were generated or analysed during the current study.

Declarations

Ethical approval This article does not contain any studies with human participants or animals performed by any of the authors. There is no ethical concern in this research.

Informed consent All the authors have been listed, and the authors have no objection for the authorship list.

Competing interests The authors declare no competing interests.

Open Access This article is licensed under a Creative Commons Attribution 4.0 International License, which permits use, sharing, adaptation, distribution and reproduction in any medium or format, as long as you give appropriate credit to the original author(s) and the source, provide a link to the Creative Commons licence, and indicate if changes were made. The images or other third party material in this article are included in the article's Creative Commons licence, unless indicated otherwise in a credit line to the material. If material is not included in the article's Creative Commons licence and your intended use is not permitted by statutory regulation or exceeds the permitted use, you will need to obtain permission directly from the copyright holder. To view a copy of this licence, visit http://creativecommons.org/licenses/by/4.0/.

References

Aghababaei, R., Reddy, J.N.: Nonlocal third-order shear deformation plate theory with application to bending and vibration of plates. J. Sound Vib. **326**, 277–289 (2009). https://doi.org/10.1016/j.jsv.2009.04.044

Alghanmi, R.A.: Nonlocal Strain Gradient Theory for the Bending of Functionally Graded Porous Nanoplates. Materials **15** (2022). https://doi.org/10.3390/ma15238601

Alghanmi, R.A.: Hygrothermal bending analysis of sandwich nanoplates with FG porous core and piezomagnetic faces via nonlocal strain gradient theory. Nanotechnol. Rev. **12** (2023). https://doi.org/10.1515/ntrev-2023-0123

Alghanmi, R.A., Zenkour, A.M.: An electromechanical model for functionally graded porous plates attached to piezoelectric layer based on hyperbolic shear and normal deformation theory. Compos. Struct. **274**, 114352 (2021). https://doi.org/10.1016/j.compstruct.2021.114352

Amini, Y., Emdad, H., Farid, M.: Finite element modeling of functionally graded piezoelectric harvesters. Compos. Struct. **129**, 165–176 (2015). https://doi.org/10.1016/j.compstruct.2015.04.011

Arefi, M., Zenkour, A.M.: A simplified shear and normal deformations nonlocal theory for bending of functionally graded piezomagnetic sandwich nanobeams in magneto-thermo-electric environment. J. Sandw. Struct. Mater. **18** (2016). https://doi.org/10.1177/1099636216652581

Arefi, M., Zenkour, A.M.: Free vibration analysis of a three-layered microbeam based on strain gradient theory and three-unknown shear and normal deformation theory. Steel Compos. Struct. **26** (2018). https://doi.org/10.12989/scs.2018.26.4.421

Arefi, M., Kiani, M., Zenkour, A.M.: Size-dependent free vibration analysis of a three-layered exponentially graded nano-/micro-plate with piezomagnetic face sheets resting on Pasternak's foundation via MCST. J. Sandw. Struct. Mater. **22**, 55–86 (2020). https://doi.org/10.1177/1099636217734279

Azzara, R., Carrera, E., Filippi, M., Pagani, A.: Vibration analysis of thermally loaded isotropic and composite beam and plate structures. J. Therm. Stresses **46**, 369–386 (2023a). https://doi.org/10.1080/01495739.2023.2188399

Azzara, R., Carrera, E., Filippi, M., Pagani, A.: Vibration analysis of thermally loaded isotropic and composite beam and plate structures. J. Therm. Stresses **46**, 369–386 (2023b). https://doi.org/10.1080/01495739.2023.2188399

Bhangale, R.K., Ganesan, N.: Static analysis of simply supported functionally graded and layered magneto-electro-elastic plates. Int. J. Solids Struct. **43**, 3230–3253 (2006). https://doi.org/10.1016/j.ijsolstr.2005.05.030

Daikh, A.A., Bachiri, A., Houari, M.S.A., Tounsi, A.: Size dependent free vibration and buckling of multi-layered carbon nanotubes reinforced composite nanoplates in thermal environment. Mech. Based Des. Struct. Mach. **50**, 1371–1399 (2022). https://doi.org/10.1080/15397734.2020.1752232

Daikh, A.A., Belarbi, M.O., Khechai, A., Li, L., Ahmed, H.M., Eltaher, M.A.: Buckling of bi-coated functionally graded porous nanoplates via a nonlocal strain gradient quasi-3D theory. Acta Mech. **234**, 3397–3420 (2023a). https://doi.org/10.1007/s00707-023-03548-9

Daikh, A.A., Belarbi, M.O., Khechai, A., Li, L., Khatir, S., Abdelrahman, A.A., Eltaher, M.A.: Bending of Bi-directional inhomogeneous nanoplates using microstructure-dependent higher-order shear deformation theory. Eng. Struct. **291** (2023b). https://doi.org/10.1016/j.engstruct.2023.116230

Ebrahimi, F., Barati, M.R.: Dynamic modeling of a thermo–piezo-electrically actuated nanosize beam subjected to a magnetic field. Appl. Phys. A, Mater. Sci. Process. **122**, 1–18 (2016a). https://doi.org/10.1007/s00339-016-0001-3

Ebrahimi, F., Barati, M.R.: Electromechanical buckling behavior of smart piezoelectrically actuated higher-order size-dependent graded nanoscale beams in thermal environment. Int. J. Smart Nano Mater. **7**, 69–90 (2016b). https://doi.org/10.1080/19475411.2016.1191556

Ebrahimi, F., Barati, M.R.: Buckling analysis of piezoelectrically actuated smart nanoscale plates subjected to magnetic field. J. Intell. Mater. Syst. Struct. **28**, 1472–1490 (2017a). https://doi.org/10.1177/1045389X16672569

Ebrahimi, F., Barati, M.R.: Vibration analysis of viscoelastic inhomogeneous nanobeams incorporating surface and thermal effects. Appl. Phys. A **123**, 5 (2017b). https://doi.org/10.1007/s00339-016-0511-z

Eringen, A.C.: Nonlocal polar elastic continua. Int. J. Eng. Sci. **10**, 1–16 (1972a). https://doi.org/10.1016/0020-7225(72)90070-5

Eringen, A.C.: Theory of micromorphic materials with memory. Int. J. Eng. Sci. **10**, 623–641 (1972b). https://doi.org/10.1016/0020-7225(72)90089-4

Eringen, A.C.: On differential equations of nonlocal elasticity and solutions of screw dislocation and surface waves. J. Appl. Phys. **54**, 4703–4710 (1983a). https://doi.org/10.1063/1.332803

Eringen, A.C.: Theories of nonlocal plasticity. Int. J. Eng. Sci. **21** (1983b). https://doi.org/10.1016/0020-7225(83)90058-7

Eringen, A.C., Edelen, D.G.B.: On nonlocal elasticity. Int. J. Eng. Sci. **10**, 233–248 (1972). https://doi.org/10.1016/0020-7225(72)90039-0

Eringen, A.C., Suhubi, E.S.: Nonlinear theory of simple micro-elastic solids—I. Int. J. Eng. Sci. **2**, 189–203 (1964). https://doi.org/10.1016/0020-7225(64)90004-7

Eringen, A., Wegner, J.: Nonlocal continuum field theories. Appl. Mech. Rev. **56**, B20–B22 (2003). https://doi.org/10.1115/1.1553434

Esen, I., Özmen, R.: Thermal vibration and buckling of magneto-electro-elastic functionally graded porous nanoplates using nonlocal strain gradient elasticity. Compos. Struct. **296** (2022a). https://doi.org/10.1016/j.compstruct.2022.115878. (A)

Esen, I., Özmen, R.: Thermal vibration and buckling of magneto-electro-elastic functionally graded porous nanoplates using nonlocal strain gradient elasticity. Compos. Struct. **296**, 115878 (2022b). https://doi.org/10.1016/j.compstruct.2022.115878

Farajpour, A., Rastgoo, A.: Influence of carbon nanotubes on the buckling of microtubule bundles in viscoelastic cytoplasm using nonlocal strain gradient theory. Results Phys. **7** (2017). https://doi.org/10.1016/j.rinp.2017.03.038

Fatih Pehlivan, I.E., Aktas, K.G.: The effect of the foam structure and distribution on the thermomechanical vibration behavior of sandwich nanoplates with magneto-electro-elastic face layers. Mech. Adv. Mat. Struct. **0**, 1–30 (2024). https://doi.org/10.1080/15376494.2024.2303377

Fu, J., Hou, Y., Zheng, M., Zhu, M.: Flexible piezoelectric energy harvester with extremely high power generation capability by sandwich structure design strategy. ACS Appl. Mater. Interfaces **12**, 9766–9774 (2020). https://doi.org/10.1021/acsami.9b21201

Gui, Y., Li, Z.: A nonlocal strain gradient shell model with the surface effect for buckling analysis of a magneto-electro-thermo-elastic cylindrical nanoshell subjected to axial load. Phys. Chem. Chem. Phys. **25**, 24838–24852 (2023). https://doi.org/10.1039/D3CP02880A

Guo, H., Zhang, J.: Expansion of Sandwich Tubes with Metal Foam Core Under Axial Compression. J. Appl. Mech. **90** (2023). https://doi.org/10.1115/1.4056686

Guo, J., He, B., Han, Y., Liu, H., Han, J., Ma, X., Wang, J., Gao, W., Lü, W.: Resurrected and tunable conductivity and ferromagnetism in the secondary growth La0.7Ca0.3MnO3 on transferred SrTiO3 membranes. Nano Lett. **24**, 1114–1121 (2024). https://doi.org/10.1021/acs.nanolett.3c03651

Hoang, N., Cong, N., Gia, D., Chi, N.: Thin-walled structures dynamical and chaotic analyses of single-variable-edge cylindrical panels made of sandwich auxetic honeycomb core layer in thermal environment. Thin-Walled Struct. **183**, 110300 (2023). https://doi.org/10.1016/j.tws.2022.110300

Hong, J., Wang, S., Qiu, X., Zhang, G.: Bending and Wave Propagation Analysis of Magneto-Electro-Elastic Functionally Graded Porous Microbeams. Crystals **12** (2022). https://doi.org/10.3390/cryst12050732

Huang, G.Y., Wang, B.L., Mai, Y.W.: Effect of interfacial cracks on the effective properties of magneto-electroelastic composites. J. Intell. Mater. Syst. Struct. **20**, 963–968 (2009). https://doi.org/10.1177/1045389X08101564

Iftimiciuc, M., Derluyn, A., Pflug, J., Vandepitte, D.: Out-of-plane compression mechanism of a novel hierarchical sandwich honeycomb core. J. Sandw. Struct. Mater. **25**, 518–536 (2023). https://doi.org/10.1177/10996362231159664

Janus-Michalska, M., Jasinska, D.: Comparative study of bending stiffness of sandwich plates with cellular cores. Sci. Lett. Univ. Rzesz. Technol. - Mech. **89**, 63–70 (2017). https://doi.org/10.7862/rm.2017.17

Joubaneh, E.F., Barry, O.R., Tanbour, H.E.: Analytical and Experimental Vibration of Sandwich Beams Having Various Boundary Conditions. Shock Vib. **2018** (2018). https://doi.org/10.1155/2018/3682370

Khan, L.A., Ali Khan, W., Ahmed, S.: Out-of-autoclave (OOA) manufacturing technologies for composite sandwich structures. In: Handb. Res. Manuf. Process Model. Optim. Strateg, pp. 292–317 (2017). https://doi.org/10.4018/978-1-5225-2440-3.ch014

Kiani, Y., Eslami, M.R.: An exact solution for thermal buckling of annular FGM plates on an elastic medium. Composites, Part B, Eng. **45**, 101–110 (2013). https://doi.org/10.1016/j.compositesb.2012.09.034

Koç, M.A., Esen, İ., Eroğlu, M.: Thermomechanical vibration response of nanoplates with magneto-electro-elastic face layers and functionally graded porous core using nonlocal strain gradient elasticity. Mech. Adv. Mat. Struct. (2023). https://doi.org/10.1080/15376494.2023.2199412

Kong, S., Zhou, S., Nie, Z., Wang, K.: The size-dependent natural frequency of Bernoulli-Euler micro-beams. Int. J. Eng. Sci. **46**, 427–437 (2008a). https://doi.org/10.1016/j.ijengsci.2007.10.002

Kong, S., Zhou, S., Nie, Z., Wang, K.: The size-dependent natural frequency of Bernoulli – Euler micro-beams. Int. J. Eng. Sci. **46**, 427–437 (2008b). https://doi.org/10.1016/j.ijengsci.2007.10.002

Kong, S., Zhou, S., Nie, Z., Wang, K.: Static and dynamic analysis of micro beams based on strain gradient elasticity theory. Int. J. Eng. Sci. **47**, 487–498 (2009). https://doi.org/10.1016/j.ijengsci.2008.08.008

Li, F., Yuan, W.: Free vibration and sound insulation of functionally graded honeycomb sandwich plates (2022)

Li, L., Hu, Y., Ling, L.: Flexural wave propagation in small-scaled functionally graded beams via a nonlocal strain gradient theory. Compos. Struct. **133**, 1079–1092 (2015). https://doi.org/10.1016/j.compstruct.2015.08.014

Li, L., Li, X., Hu, Y.: Free vibration analysis of nonlocal strain gradient beams made of functionally graded material. Int. J. Eng. Sci. **102**, 77–92 (2016). https://doi.org/10.1016/j.ijengsci.2016.02.010

Li, K., Jing, S., Yu, J., Zhang, B.: Complex Rayleigh Waves in Nonhomogeneous Magneto-Electro-Elastic Half-Spaces. Materials **14** (2021). https://doi.org/10.3390/ma14041011

Lim, C.W., Zhang, G., Reddy, J.N.: A higher-order nonlocal elasticity and strain gradient theory and its applications in wave propagation. J. Mech. Phys. Solids **78**, 298–313 (2015). https://doi.org/10.1016/j.jmps.2015.02.001

Liu, H., Lv, Z.: Vibration performance evaluation of smart magneto-electro-elastic nanobeam with consideration of nanomaterial uncertainties. J. Intell. Mater. Syst. Struct. **30**, 2932–2952 (2019). https://doi.org/10.1177/1045389X19873418

Ma, H.M., Gao, X.L., Reddy, J.N.: A microstructure-dependent Timoshenko beam model based on a modified couple stress theory. J. Mech. Phys. Solids **56**, 3379–3391 (2008). https://doi.org/10.1016/j.jmps.2008.09.007

Mahapatra, B.P., Sinha, V., Maiti, D.K., Jana, P.: Active vibration suppression of tetrachiral auxetic core sandwich panel with CFRP skin: an RVE homogenization-assisted finite element approach. Eur. J. Mech. A, Solids **106**, 105282 (2024). https://doi.org/10.1016/j.euromechsol.2024.105282

Mahesh, V.: Integrated effects of auxeticity and pyro-coupling on the nonlinear static behaviour of magneto-electro-elastic sandwich plates subjected to multi-field interactive loads. Proc. Inst. Mech. Eng., Part C, J. Mech. Eng. Sci. **237**, 3945–3967 (2023). https://doi.org/10.1177/09544062221149300

Melaibari, A., Daikh, A.A., Basha, M., Abdalla, A.W., Othman, R., Almitani, K.H., Hamed, M.A., Abdelrahman, A., Eltaher, M.A.: Free Vibration of FG-CNTRCs Nano-Plates/Shells with Temperature-Dependent Properties. Mathematics **10** (2022). https://doi.org/10.3390/math10040583

Mindlin, R.D.: Micro-structure in linear elasticity. Arch. Ration. Mech. Anal. **16**, 51–78 (1964). https://doi.org/10.1007/BF00248490

Moshtagh, E., Eskandari-Ghadi, M., Pan, E.: Time-harmonic dislocations in a multilayered transversely isotropic magneto-electro-elastic half-space. J. Intell. Mater. Syst. Struct. **30**, 1932–1950 (2019). https://doi.org/10.1177/1045389X19849286

Nouraei, M., Zamani, V.: Vibration of smart sandwich plate with an auxetic core and dual-FG nanocomposite layers integrated with piezoceramic actuators, vol. 315 (2023). https://doi.org/10.1016/j.compstruct.2023.117014

Özmen, R.: Thermomechanical vibration and buckling response of magneto-electro-elastic higher order laminated nanoplates. Appl. Math. Model. **122**, 373–400 (2023). https://doi.org/10.1016/j.apm.2023.06.005

Özmen, R., Esen, I.: Thermomechanical flexural wave propagation responses of FG porous nanoplates in thermal and magnetic fields. Acta Mech. **234**, 5621–5645 (2023). https://doi.org/10.1007/s00707-023-03679-z

Pan, E.: Exact solution for simply supported and multilayered magneto-electro-elastic plates. J. Appl. Mech. **68**, 608–618 (2001). https://doi.org/10.1115/1.1380385

Pan, E., Han, F.: Exact solution for functionally graded and layered magneto-electro-elastic plates. Int. J. Eng. Sci. **43**, 321–339 (2005). https://doi.org/10.1016/j.ijengsci.2004.09.006

Pan, E., Heyliger, P.R.: Free vibrations of simply supported and multilayered magneto-electro-elastic plates. J. Sound Vib. **252** (2002). https://doi.org/10.1006/jsvi.2001.3693

Pawlus, D.: Static Stability of Composite Annular Plates with Auxetic Properties. Materials **15** (2022). https://doi.org/10.3390/ma15103579

Qu, Y.L., Li, P., Zhang, G.Y., Jin, F., Gao, X.L.: A microstructure-dependent anisotropic magneto-electro-elastic Mindlin plate model based on an extended modified couple stress theory. Acta Mech. **231**, 4323–4350 (2020). https://doi.org/10.1007/s00707-020-02745-0

Reddy, J.N.: Energy principles and variational methods. In: Theory and Analysis of Elastic Plates and Shells (2020)

Reddy, J.N., Chin, C.D.: Thermomechanical analysis of functionally graded cylinders and plates. J. Therm. Stresses **21**, 593–626 (1998). https://doi.org/10.1080/01495739808956165

Ren, X., Das, R., Tran, P., Ngo, T.D., Xie, Y.M.: Auxetic metamaterials and structures: a review. Smart Mater. Struct. **27**, 23001 (2018). https://doi.org/10.1088/1361-665X/aaa61c

Saini, R., Pradyumna, S.: Effect of thermal environment on the asymmetric vibration of temperature-dependent two-dimensional functionally graded annular plate by Chebyshev polynomials. J. Therm. Stresses **45**, 740–761 (2022). https://doi.org/10.1080/01495739.2022.2090472

Sayyad, A.S., Avhad, P.V.: Higher-order model for the thermal analysis of laminated composite, sandwich, and functionally graded curved beams. J. Therm. Stresses **45**, 382–400 (2022). https://doi.org/10.1080/01495739.2022.2050476

Shokravi, M., Jalili, N.: Thermal dynamic buckling of temperature-dependent sandwich nanocomposite quadrilateral microplates using visco-higher order nonlocal strain gradient theory. J. Therm. Stresses **42**, 506–525 (2019). https://doi.org/10.1080/01495739.2018.1522985

Şimşek, M., Reddy, J.N.: Bending and vibration of functionally graded microbeams using a new higher order beam theory and the modified couple stress theory. Int. J. Eng. Sci. **64**, 37–53 (2013). https://doi.org/10.1016/j.ijengsci.2012.12.002

Tahir, S.I., Tounsi, A., Chikh, A., Al-Osta, M.A., Al-Dulaijan, S.U., Al-Zahrani, M.M.: An integral four-variable hyperbolic HSDT for the wave propagation investigation of a ceramic-metal FGM plate with various porosity distributions resting on a viscoelastic foundation. In: Waves in Random and Complex Media (2021). https://doi.org/10.1080/17455030.2021.1942310

Tian, R.: Dynamic crushing behavior and energy absorption of hybrid auxetic metamaterial inspired by Islamic motif art *. Appl. Math. Mech. **44**, 345–362 (2023)

Tiwari, R., Misra, J.C., Prasad, R.: Magneto-thermoelastic wave propagation in a finitely conducting medium: a comparative study for three types of thermoelasticity I, II, and III. J. Therm. Stresses **44**, 785–806 (2021). https://doi.org/10.1080/01495739.2021.1918594

Touloukian, Y.S.: Thermophysical Properties of High Temperature Solid Materials. Volume 4. Oxides and Their Solutions and Mixtures. Part 1, vol. 1. Macmillan, New York (1966)

Touloukian, Y.S.: Thermophysical Properties of High Temperature Solid Materials. Macmillan, New York (1967)

Tran, V.T., Nguyen, T.K., Nguyen, P.T.T., Vo, T.P.: Stochastic collocation method for thermal buckling and vibration analysis of functionally graded sandwich microplates. J. Therm. Stresses **46**, 909–934 (2023). https://doi.org/10.1080/01495739.2023.2217243

Vinyas, M., Kattimani, S.C.: Static analysis of stepped functionally graded magneto-electro-elastic plates in thermal environment: a finite element study. Compos. Struct. **178**, 63–86 (2017). https://doi.org/10.1016/j.compstruct.2017.06.068

Vinyas, M., Kattimani, S.C., Joladarashi, S.: Hygrothermal coupling analysis of magneto-electroelastic beams using finite element methods. J. Therm. Stresses **41**, 1063–1079 (2018). https://doi.org/10.1080/01495739.2018.1447856

Wang, X., Jin, F.: Shear horizontal wave propagation in multilayered magneto-electro-elastic nanoplates with consideration of surface/interface effects and nonlocal effects. Waves Random Complex Media **0**, 1–20 (2022). https://doi.org/10.1080/17455030.2022.2134599

Wang, B., Zhao, J., Zhou, S.: A micro scale Timoshenko beam model based on strain gradient elasticity theory. Eur. J. Mech. A, Solids **29**, 591–599 (2010). https://doi.org/10.1016/j.euromechsol.2009.12.005

Wang, Z.X., Shen, H.S., Shen, L.: Thermal postbuckling analysis of sandwich beams with functionally graded auxetic GRMMC core on elastic foundations. J. Therm. Stresses **44**, 1479–1494 (2021). https://doi.org/10.1080/01495739.2021.1994902

Wang, H., Wang, Y., Wang, B., Li, M., Li, M., Wang, F., Li, C., Diao, C., Luo, H., Zheng, H.: Significantly enhanced breakdown strength and energy density in nanocomposites by synergic modulation of structural design and low-loading nanofibers. ACS Appl. Mater. Interfaces **14**, 55130–55142 (2022). https://doi.org/10.1021/acsami.2c18113

Wang, Y., Zhu, J., Li, M., Shao, G., Wang, H., Zhang, R.: Materials & design thermal properties of high-entropy RE-disilicates controlled by high throughput composition design and optimization. Mater. Des. **236**, 112485 (2023). https://doi.org/10.1016/j.matdes.2023.112485

Wu, J., Wang, J., Xiao, D., Zhu, J.: Multiferroic and fatigue behavior of silicon-based bismuth ferrite sandwiched structure. J. Mater. Chem. **21**, 7308–7313 (2011). https://doi.org/10.1039/C0JM04026F

Wu, B., Zhang, C., Chen, W., Zhang, C.: Surface effects on anti-plane shear waves propagating in magneto-electro-elastic nanoplates. Smart Mater. Struct. **24**, 95017 (2015). https://doi.org/10.1088/0964-1726/24/9/095017

Xia, B., Huang, X., Chang, L., Zhang, R., Liao, Z., Cai, Z.: The arrangement patterns optimization of 3D honeycomb and 3D re-entrant honeycomb structures for energy absorption. Mater. Today Commun. **35**, 105996 (2023). https://doi.org/10.1016/j.mtcomm.2023.105996

Yakhno, V.G.: An explicit formula for modeling wave propagation in magneto-electro-elastic materials. J. Electromagn. Waves Appl. **32**, 899–912 (2018). https://doi.org/10.1080/09205071.2017.1410076

Yang, F., Chong, A.C.M., Lam, D.C.C., Tong, P.: Couple stress based strain gradient theory for elasticity. Int. J. Solids Struct. **39**, 2731–2743 (2002). https://doi.org/10.1016/S0020-7683(02)00152-X

Yildirim, K., Simsek, M.: Magneto-electrically induced vibration control of a plate contacted with fluid. Therm. Sci. **26**, 2973–2980 (2022). https://doi.org/10.2298/TSCI2204973Y

Yıldız, T., Esen, I.: The effect of the foam structure on the thermomechanical vibration response of smart sandwich nanoplates. Mech. Adv. Mat. Struct. **0**, 1–19 (2023). https://doi.org/10.1080/15376494.2023.2287179

Yin, D., Tang, J., Mo, R., Wang, F., Jia, X., Li, C.: Construction of Sandwich-like Structured GO/Cu2O/GO Electrochemical Biosensor for Sensitive Detection of H2O2 Releasing from Living Cells pp. 1–18 (2020)

Zhang, D.G.: Thermal post-buckling and nonlinear vibration analysis of FGM beams based on physical neutral surface and high order shear deformation theory. Meccanica **49**, 283–293 (2014). https://doi.org/10.1007/s11012-013-9793-9

Zhang, G.Y., Qu, Y.L., Gao, X.-L., Jin, F.: A transversely isotropic magneto-electro-elastic Timoshenko beam model incorporating microstructure and foundation effects. Mech. Mater. **149**, 103412 (2020a). https://doi.org/10.1016/j.mechmat.2020.103412

Zhang, X.L., Xu, Q., Zhao, X., Li, Y.H., Yang, J.: Nonlinear analyses of magneto-electro-elastic laminated beams in thermal environments. Compos. Struct. **234** (2020b). https://doi.org/10.1016/j.compstruct.2019.111524

Zhang, X., Hao, H., Tian, R., Xue, Q., Guan, H., Yang, X.: Quasi-static compression and dynamic crushing behaviors of novel hybrid re-entrant auxetic metamaterials with enhanced energy-absorption. Compos. Struct. **288**, 115399 (2022). https://doi.org/10.1016/j.compstruct.2022.115399

Zhang, W., Kang, S., Liu, X., Lin, B., Huang, Y.: Experimental study of a composite beam externally bonded with a carbon fiber-reinforced plastic plate. J. Build. Eng. **71**, 106522 (2023b). https://doi.org/10.1016/j.jobe.2023.106522

Zhang, C., Khorshidi, H., Najafi, E., Ghasemi, M.: Fresh, mechanical and microstructural properties of alkali-activated composites incorporating nanomaterials: a comprehensive review. J. Clean. Prod. **384**, 135390 (2023a). https://doi.org/10.1016/j.jclepro.2022.135390

Zhao, L., Fang, H., Wang, J., Nie, F., Li, R., Wang, Y., Zheng, L.: Ferroelectric artificial synapses for high-performance neuromorphic computing: status, prospects, and challenges. Appl. Phys. Lett. **124**, 30501 (2024). https://doi.org/10.1063/5.0165029

Zhou, L., Li, M., Cai, Y., Zhao, H., Zhao, E.: The multi-physic cell-based smoothed finite element method for dynamic characterization of magneto-electro-elastic structures under thermal conditions. Compos. Struct. **240**, 112045 (2020). https://doi.org/10.1016/j.compstruct.2020.112045

Żur, K.K., Arefi, M., Kim, J., Reddy, J.N.: Free vibration and buckling analyses of magneto-electro-elastic FGM nanoplates based on nonlocal modified higher-order sinusoidal shear deformation theory. Composites, Part B, Eng. **182** (2020). https://doi.org/10.1016/j.compositesb.2019.107601

Publisher's Note Springer Nature remains neutral with regard to jurisdictional claims in published maps and institutional affiliations.